

# Evaluation of a reduced model for investigating hurricane formation from turbulence

David A. Schechter

NorthWest Research Associates, Redmond, Washington, USA

\*Correspondence to: D. A. Schechter, NorthWest Research Associates, 4118 148th Avenue NE, Redmond, WA 98052, USA.  
E-mail: [schechter@nwra.com](mailto:schechter@nwra.com)

This paper evaluates the adequacy of a reduced (three-layer) model for understanding hurricane formation from turbulent initial conditions. The evaluation is based on a direct comparison to tropical cyclogenesis in a cloud-system-resolving (CSR) model that employs single-moment warm rain microphysics. The reduced model has three cumulus parametrizations, referred to as the convergence-based (CB), boundary layer quasi-equilibrium (BLQ), and selective boost (SB) options. Regardless of which one is activated, the reduced model produces hurricanes on the same time-scale as the CSR model. Generally speaking, the hurricanes emerge from turbulence through the coalescence and convective intensification of cyclonic vorticity. Moreover, in both the reduced and CSR models, the onset of ‘rapid intensification’ follows pronounced local growth of the  $\eta$ -variable of Ooyama (1969), which is a combined measure of deep convective instability and middle tropospheric moisture. Eliminating the surface flux of moist entropy or surface friction in either model prevents or severely inhibits hurricane formation; however, hurricanes eventually form without surface friction in the BLQ or SB versions of the reduced model.

Despite some measure of success, the reduced model has notable deficiencies that are apparent during the intermediate stage of genesis. Compared to the CSR model, rotational storms are less sporadic and their peak winds are less severe. In the intermediate mesoscale of the reduced model, the horizontal kinetic energy spectrum is relatively steep, and horizontal divergence is relatively weak. Furthermore, the Lagrangian autocorrelation time of vertical vorticity is relatively long. These discrepancies reflect a simplified (quasi-two-dimensional) form of rotational convective turbulence. The simplified turbulence has comparatively robust mesoscale vortices, and tends to produce more tropical cyclones than its counterpart generates in the CSR model. Copyright © 2011 Royal Meteorological Society

*Key Words:* tropical cyclogenesis; atmospheric modelling; vortex dynamics; convection

*Received 20 April 2010; Revised 10 September 2010; Accepted 19 October 2010; Published online in Wiley Online Library 19 January 2011*

*Citation:* Schechter DA. 2011. Evaluation of a reduced model for investigating hurricane formation from turbulence. *Q. J. R. Meteorol. Soc.* 137: 155–178. DOI:10.1002/qj.729

## 1. Introduction

Despite decades of research, hurricane formation is not fully understood. State-of-the-art, cloud-system-resolving (CSR) models are commonly used to investigate the process, but are computationally expensive and difficult to interpret. In principle, reduced models can be used to clarify the essential dynamics, and to efficiently discover new phenomena. The

primary purpose of this paper is to evaluate the use of a reduced model to understand the transformation of turbulent flows into tropical cyclones.

There are many reduced models to evaluate, each having many adjustable parameters. The present study is by no means comprehensive, but focuses on a familiar three-layer model with typical settings and three alternative cumulus parametrizations. One parametrization

is a minor variant of the classic convergence-based scheme of Ooyama (1969; henceforth O69), originally proposed for the purpose of understanding the intensification and steady-state maintenance of an isolated tropical cyclone. Another parametrization regulates convective activity through the principle of boundary-layer quasi-equilibrium (cf. Raymond, 1995; Emanuel, 1995a; Zehnder, 2001). A third resembles the convergence-based parametrization, but boosts convection in regions of exceptionally high instability.

The reduced model is evaluated, for each cumulus parametrization, by direct comparison to tropical cyclogenesis in the Regional Atmospheric Modeling System (RAMS; Cotton *et al.*, 2003). Although RAMS has two-moment microphysics with icy hydrometeors, the present study activates only single-moment warm rain microphysics. Furthermore, the surface flux parametrization is simplified to conform with the reduced model. While direct comparison of one reduced model to another has precedents (e.g. Zehnder, 2001; Zhu *et al.*, 2001; Zhu and Smith, 2002), direct comparison to a CSR model has been largely neglected. Another distinguishing feature of the present comparison is the starting point – a disorganized state of rotational moist-convective turbulence, as opposed to a weak axisymmetric cyclone or a synoptic-scale dipole.

In general, a reduced model is not a rigorous approximation of the full equations of motion. Therefore, it is unreasonable to expect precise agreement between a reduced model and a CSR numerical simulation. Nevertheless, CSR simulations and basic theoretical considerations have established minimal criteria that a reduced model should satisfy to have relevance. Two of the least controversial are:

(i) Tropical cyclogenesis must not occur solely through the conversion of ambient Convective Available Potential Energy (CAPE) into a warm core cyclone, but through an air–sea interaction instability (Rotunno and Emanuel, 1987; henceforth RE87). Consequently, the rate of tropical cyclogenesis should increase from zero with the surface exchange coefficient of moist entropy  $C_E$ . Furthermore, tropical cyclogenesis in a low-shear environment should accelerate with increasing sea-surface temperature (SST), all else being equal.

(ii) The intensity of a mature tropical cyclone should typically increase with the sea-surface temperature, and asymptotically tend to zero with the ratio of  $C_E$  to the surface drag coefficient,  $C_D$ .\*

The literature contains ample evidence that previous versions of the reduced model used here satisfy criteria (i) and (ii) (e.g. O69; DeMaria and Pickle, 1988 (DP88); Schecter and Dunkerton, 2009 (SD09); Schecter, 2010 (S10)). Therefore, the present paper does not dwell on these issues.

\*Traditional hurricane theory and modelling studies suggest that the maximum wind speed increases appreciably with the ratio  $C_E/C_D$  (e.g. Emanuel, 1986 (E86); Emanuel, 1995b; Braun and Tao, 2000). Recent CSR simulations and theoretical considerations suggest less sensitive (and sometimes opposite) sensitivity to realistic variation of  $C_D$  (Smith *et al.*, 2008 (SMV08); Smith and Montgomery, 2008 (SM08); Bryan and Rotunno, 2009a (BR09a); Montgomery *et al.*, 2010 (MSN10)). Nevertheless, the author is unaware of any credible reports contradicting the intuitively agreeable assertion made here that hurricane intensity vanishes asymptotically as either  $C_E$  approaches zero or  $C_D$  approaches infinity.

On the other hand, the literature does not contain a thorough evaluation of the chaotic flow statistics of the reduced model during genesis. Such statistics include the spectral distributions of horizontal kinetic energy, relative vorticity and horizontal divergence. If the reduced model cannot reproduce the statistics of turbulence in the intermediate mesoscale of the RAMS simulation, the adequacy of the model would be questionable. Discrepancies could indicate inaccurate convective forcing by the cumulus parametrization, incorrect mechanisms of mode-to-mode energy transfer, etc. Moreover, improper modelling of 10–100 km scale ‘fluctuations’ could substantially affect the statistics of hurricane formation, such as the mean and standard deviation for the time of genesis.

Of further interest is the evolution of the thermodynamic  $\eta$ -variable prior to the intensification of an incipient hurricane. The value of  $\eta$  is a combined measure of deep convective instability and middle tropospheric moisture. The reduced model under consideration theoretically requires that  $\eta$  exceed a finite threshold *within the storm* for the possibility of intensification (O69; SD09). In our reduced simulations, the time series of  $\eta$  in an incipient hurricane spikes well above this threshold at the onset of rapid wind speed acceleration. If  $\eta$  fails to exhibit pronounced growth prior to intensification in RAMS, a significant feature of hurricane formation in the reduced model would have dubious credibility.

The final issue under present consideration is the influence of surface friction on tropical cyclogenesis. To date, the literature presents an ambiguous truth on the subject. Two frequently cited studies, based on a standard axisymmetric cloud model, suggest that increasing the surface drag coefficient  $C_D$  from zero to a realistic value decelerates vortex intensification (Craig and Gray, 1996; Gray and Craig, 1998 (GC98)). More recent studies based on axisymmetric and fully three-dimensional (3D) models present cases with the opposite behaviour (Fang *et al.*, 2009 (FTW09); MSN10). The RAMS simulations carried out for this paper show that genesis (within one month) over a relatively cool ocean requires non-zero  $C_D$ , and that increasing  $C_D$  (to a realistic value) accelerates the process. We take this result as a provisional truth for the purpose of evaluating the reduced model. It will be shown that not all cumulus parametrizations are entirely consistent with the assumed ‘truth’.

The remainder of this paper is organized as follows. Section 2 briefly describes tropical cyclogenesis in RAMS. Section 3 presents the reduced model under evaluation for its ability to simulate the same process. Section 4 compares the reduced model to RAMS. Section 5 grades the reduced model based on past and present findings.

## 2. RAMS-6.0 simulations of tropical cyclogenesis

Idealized numerical studies of tropical cyclone development commonly start with an axisymmetric tropical depression in gradient-wind balance. Less frequently, they begin with a random temperature perturbation in a resting atmosphere. The buoyancy field associated with the temperature perturbation initiates rotational convection, which evolves into numerous mesoscale convective vortices. Here, we take the middle road, and start with a balanced flow field resembling a random distribution of lower-tropospheric vortices.

The simulations are carried out with the Regional Atmospheric Modeling System (RAMS-6.0; Cotton *et al.*, 2003). For simplicity, we activate only single-moment, warm-rain microphysics and the Mahrer–Pielke long wave radiation scheme. The standard surface flux parametrization is simplified to resemble that of the reduced model. Appendix A provides details of the modification, and evidence of its proper implementation. The sea-surface temperature  $T_s$  and Coriolis parameter  $f$  are held constant. The horizontal domain is a  $2000 \times 2000$  km periodic box. The upper boundary is a rigid lid roughly 22 km from the sea surface, but a linear sponge layer damps upward propagating gravity waves above 15 km. The horizontal resolution is 3.9 km, and the vertical mesh contains 33 stretched grid points. In the lowest 1 km of the troposphere, the vertical resolution varies from 196 to 256 m. The computational resolution is crude by modern standards, but seems adequate for basic comparison to a three-layer model.

### 2.1. Genesis over a cool ocean at $10^\circ\text{N}$

To begin with, we consider a RAMS simulation of tropical cyclogenesis over a 'cool' ocean ( $T_s = 26^\circ\text{C}$ ) at about  $10^\circ\text{N}$  ( $f = 2.5 \times 10^{-5}\text{s}^{-1}$ ). The ambient temperature and moisture fields of the atmosphere are initialized with the Jordan (1958) mean sounding for the West Indies during hurricane season. Appendix B explains how balanced turbulence is superposed on the ambient conditions in the lower troposphere. Above 6 km, the atmosphere is initially at rest.

Figure 1(a) shows the evolution of the velocity and precipitation fields during hurricane formation. Figure 2 (top) shows the evolution of relative vorticity in the 'boundary layer', here defined as the lowest 1 km of the atmosphere. The snapshots illustrate distinct stages of the transformation from turbulence to hurricane, but do not tell the complete story. The early stage involves 2D processes of self-organization, such as the coalescence of like-sign vorticity through mergers and more subtle mechanisms (Melander *et al.*, 1988; Carnevale *et al.*, 1991; Dritschel and Waugh, 1992; Lansky *et al.*, 1997; Schecter and Dubin, 1999, 2001; Schecter, 2003). Mesoscale cyclones progressively dominate anticyclones. Sporadic convection occurs within larger mesoscale structures, creating new mesocyclones. Eventually, a domain-scale cyclonic circulation develops. The subsequent evolution appears similar to that discussed and analysed elsewhere in much greater detail (e.g. Hendricks *et al.*, 2004; Reasor *et al.*, 2005; Montgomery *et al.*, 2006; Nolan, 2007; Nolan *et al.*, 2007; Nguyen *et al.*, 2008; Houze *et al.*, 2009; Fang and Zhang, 2010; Tory and Frank, 2010). Strong mesovortices occasionally appear, and sometimes merge, until one becomes the core of an incipient hurricane. The core rapidly intensifies as it moves toward and becomes the centre of the broader circulation. Section 4.4 will discuss notable indicators for the onset of this event. During intensification, the core develops a prominent eye and eyewall (cf. Shapiro and Willoughby, 1982 (SW82); Wirth and Dunkerton, 2009). The mature hurricane is generally consistent with that found in other CSR models and observations (section 4.5; Appendix C; RE87; Houze, 1993 (H93); Liu *et al.*, 1997, 1999; Montgomery *et al.*, 2006).

Appendix C illustrates how the basic state of the developing hurricane evolves from a conditionally unstable

configuration to one with slantwise convective neutrality in the eyewall. The initial CAPE (or slantwise-CAPE) inside the vortex may help stimulate intensification, but the process is essentially an air–sea interaction instability (RE87). The author has verified that extinguishing the sea surface fluxes of latent and sensible heat arrests intensification in this simulation.

It is worth noting that the domain-average sounding of the atmosphere changes appreciably during the simulation, due to the combined effects of convection and radiation. Figure 3 compares the sounding between days 3 and 10 of tropical cyclogenesis to the initial Jordan sounding. The entire troposphere cools and the lower troposphere dries, but the ambient CAPE increases from 1830 to  $2541 \text{ J kg}^{-1}$ .<sup>†</sup> The modified sounding is not entirely realistic, but the simulation suffices for the study of fundamental processes, and for comparison to reduced models with similar conditions.

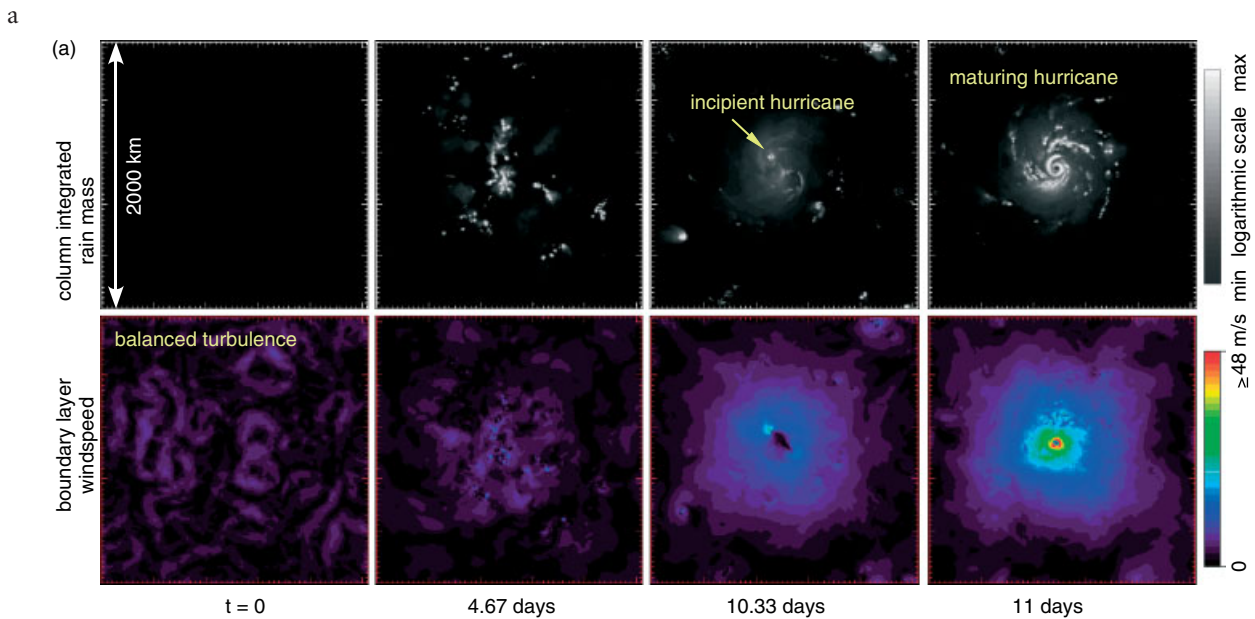
### 2.2. The consequence of removing surface drag

Figure 4 shows the maximum horizontal wind speed in the boundary layer *versus* time for several RAMS simulations of turbulent convection over a cool ocean at  $10^\circ\text{N}$ . The solid curve corresponds to the control simulation, in which hurricane formation occurs. The broken curves correspond to modified runs in which surface drag is artificially removed before (dashed) or shortly after (dotted) the incipient hurricane of the control run appears. Although  $C_D$  becomes zero, the wind-induced surface fluxes of sensible and latent heat continue as usual. Initially, eliminating surface drag has little effect on the acceleration of wind speed. However, removing the influence of surface drag on boundary layer convergence and convective organization ultimately inhibits hurricane formation. The insets of Figure 4 show the patterns of convection when the curves are terminated on the plot, and verify the absence of tropical cyclones when  $C_D$  is zero. The simulation corresponding to the dotted curve was actually carried out until day 30, with no sign of hurricane formation. We note that increasing  $C_D$  from zero to one-half of the control value suffices to generate a tropical cyclone with sustained hurricane-strength winds after 25 days (not shown).

Despite having profound impact on the emergence of a hurricane in our numerical experiment, surface drag appears to have little direct influence on daily precipitation during the intermediate phase of tropical cyclogenesis. Figures 5(a, b) show a 3D visualization of the convection, and the column-integrated rain mass  $P_c$ , at 4.33 days into the simulation.<sup>‡</sup> Figure 5(c) shows the average of  $P_c$  over 49 snapshots, taken at 30 min intervals from this time. Figures 5(d, e) show similar daily averages without surface drag, and without sea surface fluxes of latent and sensible heat. Removing surface drag has negligible

<sup>†</sup>All values of CAPE in this paper correspond to the column maximum, computed by the IDL routine 'cape\_sound', which is based on Emanuel's 'calcsound' (Emanuel, 1994; D. Brunner, 2004, [http://www.iac.ethz.ch/staff/dominik/idltools/idl\\_atmosphs.html](http://www.iac.ethz.ch/staff/dominik/idltools/idl_atmosphs.html)).

<sup>‡</sup>For all calculations in this paper, the column-integrated rain mass is defined by the formula  $P_c \equiv d^2 \int r_r \rho \, dz$ , in which  $r_r$  is the mixing ratio of rain,  $\rho$  is the mass density of the gaseous component of air,  $d$  is the horizontal grid increment, and the integral covers the entire vertical extent of the simulation domain. Using  $\rho$  instead of the dry mass density  $\rho_d$  results in an error of no more than 2%.



**Figure 1a.** The precipitation field and boundary layer wind speed in a RAMS simulation of tropical cyclogenesis over an ocean with  $T_s = 26^\circ\text{C}$  at  $10^\circ\text{N}$ . The column-integrated rain mass is plotted with a logarithmic greyscale, whose darkest shade is four orders of magnitude below the instantaneous maximum. The boundary layer wind speed is plotted with a linear, time-invariant colour shading.

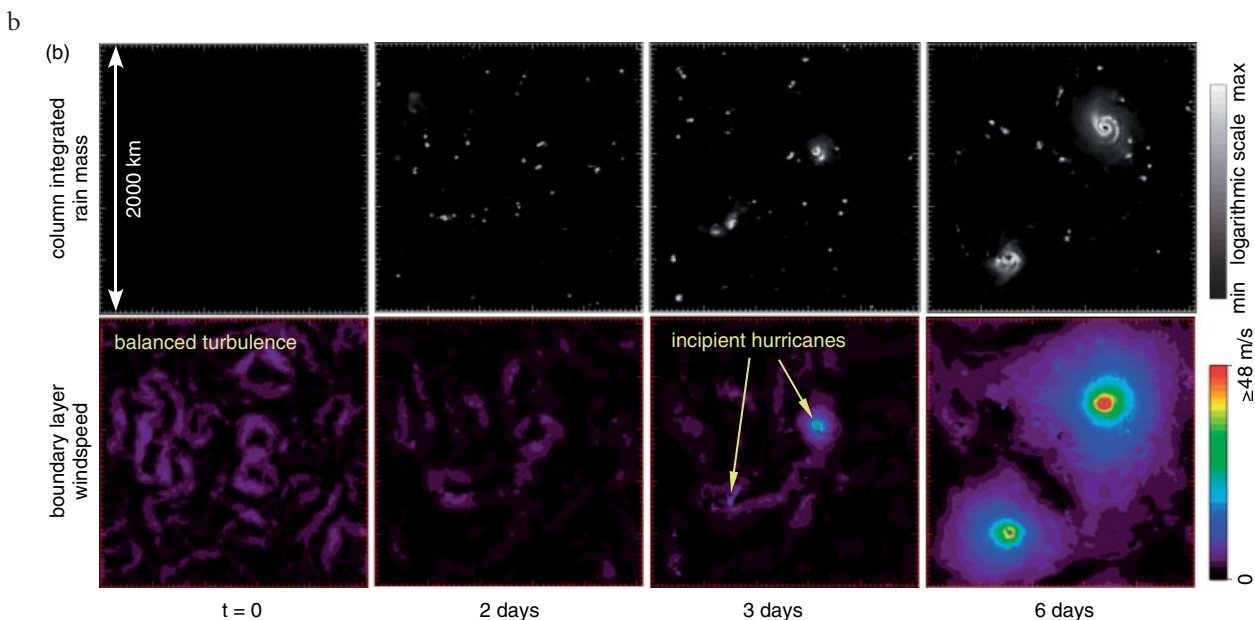


**Figure 1b.** As (a), but over an ocean with  $T_s = 29^\circ\text{C}$  at  $10^\circ\text{N}$ .

consequence on the pattern of convection, but increases the total precipitation by a factor of 1.09. Extinguishing the surface fluxes of sensible heat and moisture does not critically alter the progression of precipitation waves or the sporadic development of convection in regions of relatively high CAPE during this time period. However, deep convection is noticeably less pervasive, and the total precipitation decays by a factor of 0.51. Figures 5(f)–(k) show the continued evolution of the precipitation fields. The influence of surface drag remains minimal 7.33 days into genesis, but seems to nudge convection toward the centre of the developing domain-scale circulation. By contrast, precipitation is virtually quenched by this time without surface fluxes of sensible and latent heat to restore moist entropy in the lower troposphere.

### 2.3. Genesis over a warm ocean at $10^\circ\text{N}$

Before moving on, it is worth noting that some elements of genesis over a cool ocean are not universal. Figure 1(b) shows the evolution of the velocity and precipitation fields for a RAMS simulation in which  $T_s = 29^\circ\text{C}$ , and the Coriolis parameter is representative of  $10^\circ\text{N}$ . Figure 2 (bottom) shows the corresponding evolution of relative vorticity in the boundary layer. In this case, two incipient hurricanes rapidly form in larger mesoscale regions of cyclonic vorticity. The storms mature into full-strength hurricanes well before a domain-scale circulation has time to develop. Quasi-2D principles of organization, such as coalescence of cyclonic vorticity through merger, appear much less relevant to the process, at least on the 100 km mesoscale.

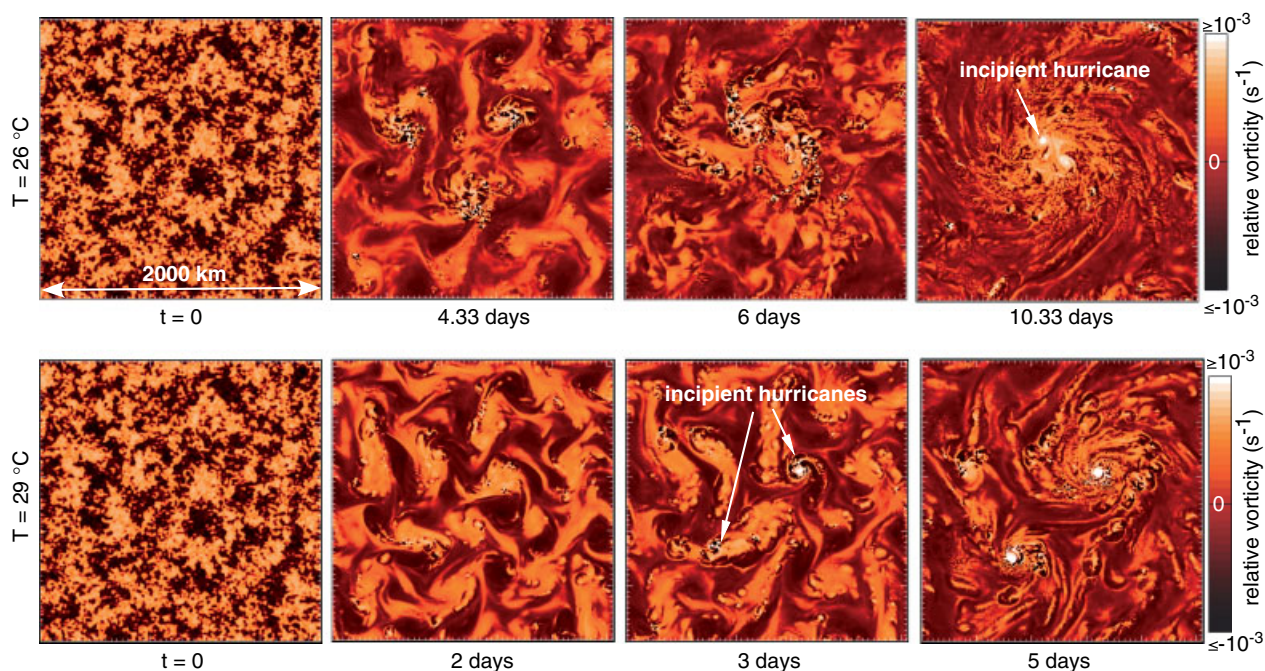


**Figure 2.** Relative vorticity  $\zeta$  of the boundary layer in RAMS simulations of tropical cyclogenesis over oceans with (upper row)  $T_s = 26^\circ\text{C}$  and (lower row)  $T_s = 29^\circ\text{C}$ . The positive and negative halves of the colour scale are scaled logarithmically from  $10^{-6}$  to  $10^{-3}\text{s}^{-1}$ . Grid points with  $|\zeta| \leq 10^{-6}\text{s}^{-1}$  are coloured with the central shade of red.

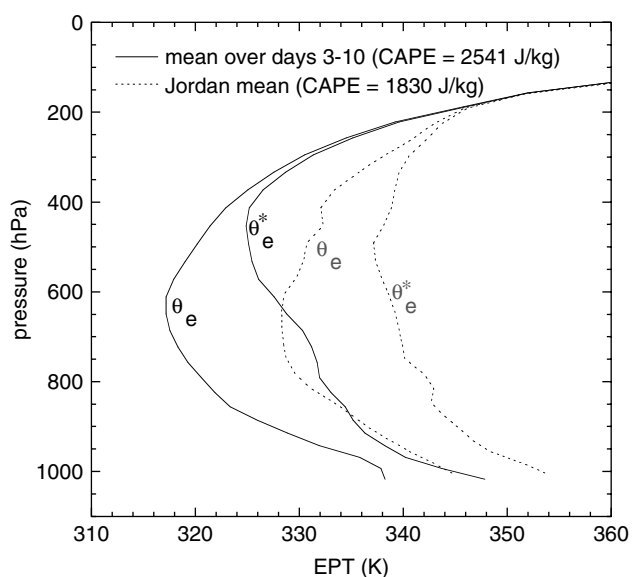


**Figure 3.** The 3–10 day vertical profile of the domain-averaged EPT and saturation EPT in a RAMS simulation, compared to the initial profiles taken from Jordan (1958).

Faster genesis over a warmer ocean is not surprising, when other factors are not considered. In some scenarios, attendant warming of the ambient upper troposphere or introduction of vertical wind shear could impede genesis. Those interested in comprehensive discussions of the environmental conditions that promote hurricane formation and intensification may consult an extensive body of literature on the topic (e.g. Gray, 1968; DeMaria *et al.*, 2001, 2005; Kaplan and DeMaria, 2003 (KD03); Carmago *et al.*, 2007a,b; Nolan *et al.*, 2007; Nolan and Rappin, 2008; Dunkerton *et al.*, 2009; Tory and Frank, 2010). A lengthy review is beyond the scope of this paper.

### 3. The reduced model

The primary issue under consideration is the ability of a reduced model to simulate tropical cyclogenesis consistently with RAMS. Here, we examine a reduced model of the tropical troposphere that consists of two ‘shallow-water’ layers over a thin boundary layer (cf. SD09). As in RAMS, the underlying ocean supplies moist entropy and exerts surface drag. Deep cumulus convection is represented by the rarefaction of lower-tropospheric air, and its elevation into the upper layer. In general, the intensity of deep convection depends on the local sounding, the local surface flux of moist entropy, and the local convergence of boundary layer air. The nature of each dependency varies with the cumulus parametrization. In two of the three cumulus parametrizations under consideration, ‘precipitation-cooled’ downdraughts into the boundary layer accompany deep convection. Radiation effects are crudely incorporated into the model through subsidence of condensed upper-tropospheric air into the middle layer, and relaxation of entropy variables toward their rest values.

The following describes the mathematical structure of the reduced model in some detail. The dynamical core consists of prognostic equations for the horizontal velocity  $\mathbf{u}$  of each layer, and the thickness  $h$  of the middle and upper layers. The cumulus parametrizations involve prognostic equations for the EPTs of the boundary and middle layers, and a diagnostic equation for the saturation EPT of the upper layer. Readers interested in the historical use of similar three-layer models to elucidate the dynamics of hurricanes or midlatitude vortices may consult numerous references on the subject (O69; DeMaria and Schubert, 1984; DP88; Shapiro, 1992, 2000; Dengler and Reeder, 1997; Zehnder, 2001; Zhu *et al.*, 2001; Zhu and Smith, 2002; Arakawa, 2004; Lapeyre and Held, 2004; SD09). A complimentary body of literature demonstrates the use of reduced models to understand tropical waves and generic patterns of tropical

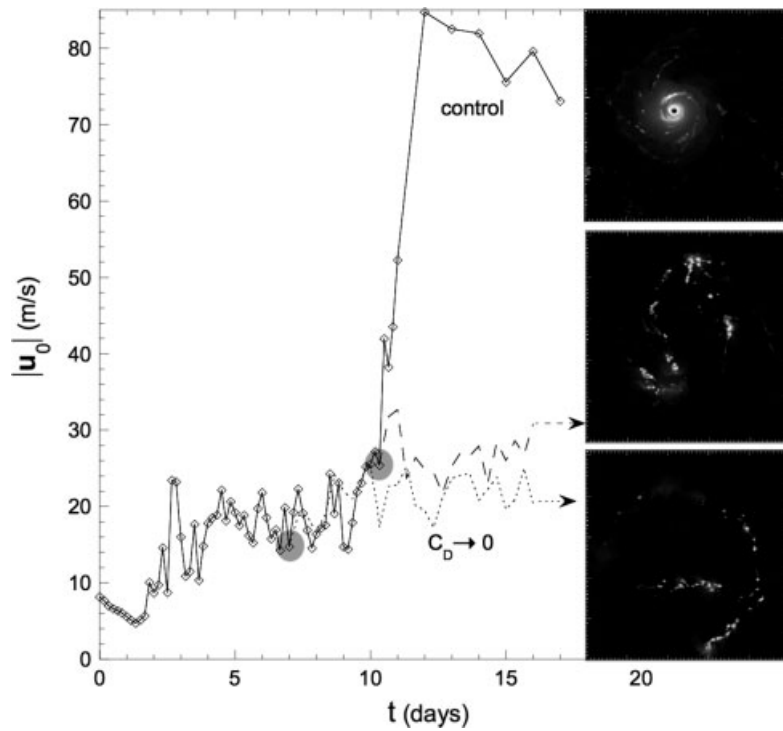


**Figure 4.** Time series of the domain-maximum boundary layer wind speed in one successful and two unsuccessful RAMS simulations of hurricane formation ( $T_s = 26^\circ\text{C}$ ). The solid curve denotes the control simulation, which has surface drag. The broken curves denote simulations in which surface drag is removed at the points indicated by shaded circles. The insets show the column-integrated rain mass (in the entire domain) at the end of each simulation. The grey scale is logarithmic, with light/dark shades representing high/low precipitation.

convection (Crum and Dunkerton, 1992,1993; Yano *et al.*, 1995; Mapes, 2000; Frierson *et al.*, 2004; Khouider and Majda, 2007; Bouchut *et al.*, 2009).

3.1. Mass and momentum equations

The mass continuity equation for layer  $m$  has the general form

$$\begin{aligned} \partial_t h_m + \nabla \cdot h_m \mathbf{u}_m = & \sum_l (\epsilon_{lm} Q_{lm}^c - Q_{ml}^c) \\ & + \sum_l (\epsilon_{lm} Q_{lm}^r - Q_{ml}^r), \end{aligned} \quad (1)$$

in which  $l, m \in \{0, 1, 2\}$ ,  $\epsilon_{lm} \equiv \rho_l / \rho_m$ ,  $\rho_l$  is the mass density of layer  $l$ ,  $Q_{lm}^c$  is the mass flux (divided by  $\rho_l$ ) from layer  $l$  to  $m$  due to convection,  $Q_{lm}^r$  is a similar mass flux nominally due to radiative cooling, and  $\nabla$  is the horizontal gradient operator. The momentum equations have the general form

$$\begin{aligned} \partial_t \mathbf{u}_m + \mathbf{u}_m \cdot \nabla \mathbf{u}_m = & \\ -\nabla \phi_m - f \hat{\mathbf{z}} \times \mathbf{u}_m + \sum_l \frac{\epsilon_{lm}}{h_m} (Q_{lm}^c + Q_{lm}^r) (\mathbf{u}_l - \mathbf{u}_m) + \mathbf{F}_m, \end{aligned} \quad (2)$$

in which  $\nabla \phi_m$  is the hydrostatic pressure gradient,  $f$  is the (constant) Coriolis parameter,  $\hat{\mathbf{z}}$  is the vertical unit vector,

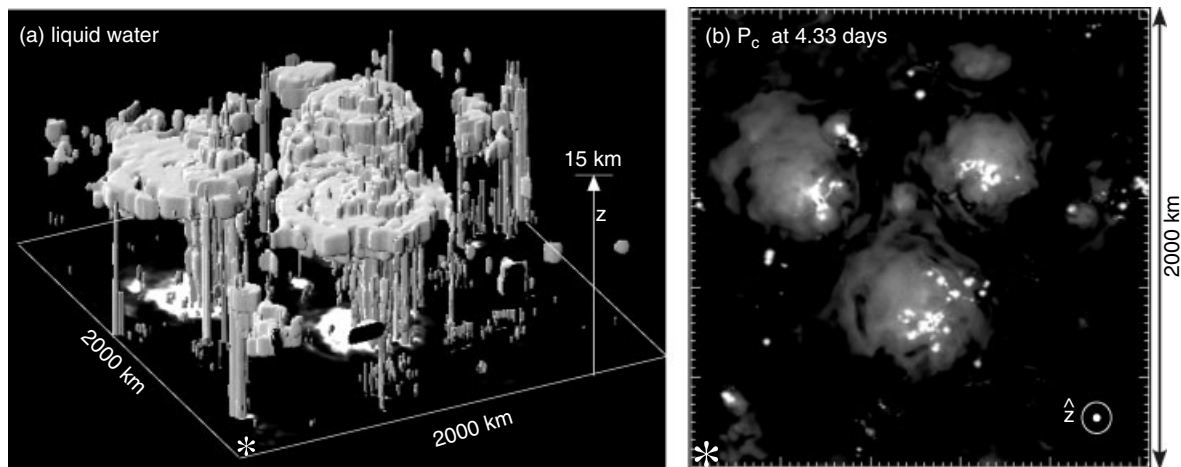


**Figure 5.** Moist convection during the intermediate stage of tropical cyclogenesis in a RAMS simulation. (a) An isosurface of the total liquid mixing ratio ( $\eta = 10^{-5}$ ) enclosing much of the liquid water mass at  $t = 4.33$  days. The white area on the base of the figure where  $\eta \geq 10^{-6}$  at an altitude of 98.2 m above sea level. For perspective, the peak value of  $\eta$  is 0.0144 at this time. (b) The column-integrated rain mass ( $P_c$ ) at  $t = 4.33$  days. The shading covers four orders of magnitude on a logarithmic grey scale, with lighter shades representing greater rain mass. The asterisks in (a) and (b) mark a common point of reference.

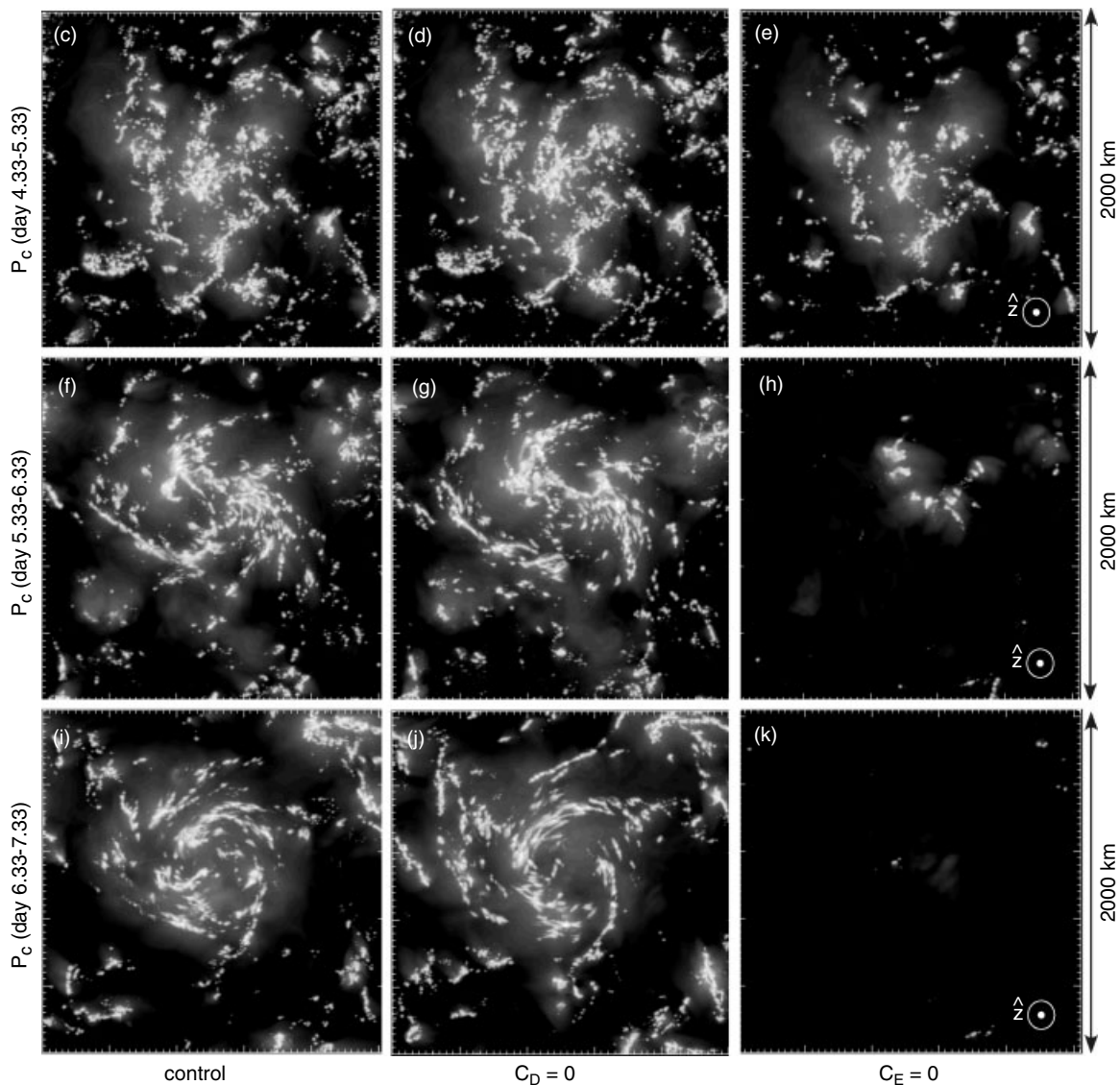


**Figure 5.** (c) The one-day average of  $P_c$  starting at  $t = 4.33$  days, for the control simulation in which all surface fluxes are activated. (d) The same one-day average of  $P_c$  without surface drag. The area integral of  $P_c$  in (d) is 1.09 times that of the control run. (e) The same one-day average of  $P_c$  with surface drag, but without surface fluxes of sensible and latent heat. The area integral of  $P_c$  in (e) is 0.51 times that of the control run. (f)–(h) are as (c)–(e), but starting at  $t = 5.33$  days. The area integrals of  $P_c$  in (g) and (h) are 1.07 and 0.09 times that of (f), respectively. (i)–(k) are as (c)–(e), but starting at  $t = 6.33$  days. The area integrals of  $P_c$  in (j) and (k) are 1.06 and 0.003 times that of (i), respectively. The grey scales in (c)–(k) are exactly the same as in (b).

and  $\mathbf{F}_m$  represents surface friction, interface friction, and lateral eddy viscosity. For simplicity we assume that  $\rho_0 = \rho_1$ . Therefore, all elements of the mass matrix are unity except  $\epsilon_{20} = \epsilon_{21} \equiv \epsilon$ , and  $\epsilon_{02} = \epsilon_{12} \equiv \epsilon^{-1}$ . In addition, we assume that the positive and negative mass fluxes into the boundary layer cancel at each point in space, such that  $h_0$  is constant and its prognostic equation is eliminated from the model. Under these special conditions, we also have

$$\begin{aligned} \phi_0 = \phi_1 &\equiv g(h_1 - H_1) + \epsilon g(h_2 - H_2), \\ \phi_2 &\equiv g(h_1 - H_1) + g(h_2 - H_2), \end{aligned} \quad (3)$$

in which  $g$  is gravitational acceleration and  $H_m$  is the initial domain average of  $h_m$ .

### 3.2. Friction

The frictional term in the momentum equation has the form

$$\begin{aligned} \mathbf{F}_m = -C_D |\mathbf{u}_0| \frac{\mathbf{u}_0}{H_0} \delta_{0m} + \frac{\mu \epsilon_{0m}}{h_m} \sum_{l=m\pm 1} (\mathbf{u}_l - \mathbf{u}_m) \\ + \frac{1}{h_m} \nabla \cdot [v(\mathbf{u}_m) h_m \mathbf{\Xi}_m]. \end{aligned} \quad (4)$$

Here,  $\delta_{lm}$  is the Kronecker-delta tensor,  $\mu$  is a small constant of interface friction, and the sum is over all layers adjacent to  $m$ . If  $m = 0$  or  $m = 2$ , then  $l = -1$  or  $l = 3$  are excluded from the sum. The formula for the surface momentum exchange coefficient is given by (cf. RE87)

$$C_D = C_{D*} (a + b |\mathbf{u}_0|), \quad (5)$$

in which  $a = 0.0011$ ,  $b = 4 \times 10^{-5} \text{ m s}^{-1}$ , and  $C_{D*}$  is an adjustable constant. Dropping the layer subscript, lateral eddy viscosity is represented by the inverse of  $h$  times the divergence of the stress tensor  $vh\mathbf{\Xi}$ . As in SD09, we let

$$\nabla \cdot vh\mathbf{\Xi} \equiv \sum_{i,j} \partial_j [vh(\partial_i u_j + \partial_j u_i)] \hat{\mathbf{x}}_i,$$

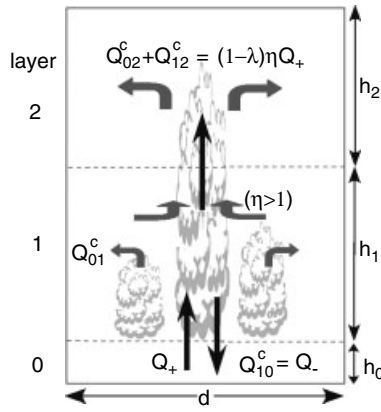


**Figure 6.** Cartoon of the mass flow associated with cumulus convection within a three-layer grid column of the reduced model. Here, the cell-averaged EPT of the boundary layer  $\theta_{e0}$  exceeds the saturation EPT of the upper layer  $\theta_{e2}^*$ , such that the entrainment parameter  $\eta$  exceeds unity.  $Q_{lm}^c$  denotes the cumulus mass flux from layer  $l$  to  $m$ , divided by the mass density  $\rho_l$ .

in which  $\partial_i$  is the partial derivative with respect to the horizontal Cartesian coordinate  $x_i$ ,  $\hat{x}_i$  is the unit vector parallel to the  $x_i$ -axis,  $u_i$  is the  $x_i$ -component of  $\mathbf{u}$ , and the sum runs over all combinations of  $i, j \in \{1, 2\}$ . Unlike SD09, the viscosity coefficient depends on the local deformation rate as follows:

$$v(\mathbf{u}) = \xi d^2 \sqrt{\sum_{i,j} (\partial_i u_j + \partial_j u_i)^2}, \quad (6)$$

in which  $\xi$  is a constant much less than unity,  $d$  is the characteristic subgrid eddy-scale (one horizontal grid increment), and the sum is again over all combinations of  $i$  and  $j$ .

### 3.3. Cumulus parametrization

The cumulus parametrization is fairly simple (Figure 6). In general, each atmospheric column has a cumulus updraught and associated downdraught at the flat interface between the boundary and middle layers. The magnitudes of the upward and downward mass fluxes are  $\rho_0 Q_+$  and  $\rho_0 Q_-$ , respectively. The updraught may entrain low-entropy air from the middle layer as it ascends into the upper layer. Assuming that the entropy of a mixed parcel equals the saturation entropy of the upper layer, the mass ratio of middle to boundary layer air in the mixed updraught is  $(\eta - 1) : 1$  (O69). Here, we have introduced the local entrainment parameter,

$$\eta \equiv 1 + \frac{\theta_{e0} - \theta_{e2}^*}{\theta_{e2}^* - \theta_{e1}^*}, \quad (7)$$

in which  $\theta_{em}$  represents the equivalent potential temperature (EPT) of layer  $m$ , and the asterisk denotes the saturation EPT. The value of  $\eta$  may be viewed as a combined measure of deep convective instability and middle tropospheric moisture. If all of the moist air from the boundary layer contributes to deep cumulus convection, then the total cumulus mass flux at the free interface between the middle and upper layers would be  $M_c = \eta \rho_0 Q_+$ . Instead, we allow a constant mass fraction  $\lambda$  of boundary layer air to detrain into the middle layer, so that  $M_c = \eta(1 - \lambda)\rho_0 Q_+$ . The value of  $M_c$  may be viewed as a conversion rate (per unit area) of dense air

into rarefied air due to cumulus convection. A net gain of low-density air (which requires non-zero  $M_c$ ) is analogous to warming of the local atmospheric column (O69).

The above picture applies only where  $\eta > 1$ , or where the EPT of the boundary layer exceeds the saturation EPT of the upper layer. Under more stable conditions, one might suppose that all of the air from the boundary layer detrains into the middle layer. But this would mean  $M_c$  drops discontinuously to zero as  $\eta$  passes below unity. A discontinuity of this kind does not seem physical, nor is it welcome in a numerical model. Instead, we smooth the discontinuity by extending the formula  $M_c = \eta(1 - \lambda)\rho_0 Q_+$  to values of  $\eta$  between unity and zero. Furthermore, we extend to this regime the condition at  $\eta = 1$  of no entrainment into the updraught. It follows that, for  $0 \leq \eta < 1$ , the mass fraction of boundary layer air detrained into the middle layer is given by  $1 - \eta(1 - \lambda)$ . The minimum and maximum values of the detrained mass fraction are  $\lambda$  and 1, at  $\eta = 1$  and  $\eta = 0$  respectively.

Translating the above discussion into an equation for  $\mathbf{Q}^c$  yields

$$\mathbf{Q}^c \equiv \begin{pmatrix} Q_{00}^c & Q_{01}^c & Q_{02}^c \\ Q_{10}^c & Q_{11}^c & Q_{12}^c \\ Q_{20}^c & Q_{21}^c & Q_{22}^c \end{pmatrix} = \begin{pmatrix} 0 & \{1 - \eta(1 - \lambda), \lambda\} \eta Q_+ & \{\eta(1 - \lambda), (1 - \lambda)\} \eta Q_+ \\ Q_- & 0 & \{0, (\eta - 1)(1 - \lambda)\} \eta Q_+ \\ 0 & 0 & 0 \end{pmatrix}. \quad (8)$$

Here we have introduced the notation  $\{a, b\}_\eta$  to represent  $a$  or  $b$  if  $\eta$  is less than or greater than unity, respectively.

Mass conservation in each material element of boundary layer air requires that  $Q_-$  and  $Q_+$  in Eq. (8) satisfy

$$Q_- - Q_+ = H_0 \nabla \cdot \mathbf{u}_0, \quad (9)$$

assuming  $Q_{l0}^c = Q_{0l}^c = 0$ . This constraint is an important feature of the model. Its removal would require a deformable interface between the boundary and middle layers.

Evaluation of  $\eta$  requires knowledge of several EPTs. The boundary layer EPT is governed by

$$\partial_t \theta_{e0} + \mathbf{u}_0 \cdot \nabla \theta_{e0} = C_E |\mathbf{u}_0| \frac{\theta_{es}^* - \theta_{e0}}{H_0} + Q_{10}^c \frac{\theta_{e1} - \theta_{e0}}{H_0} + \frac{\bar{\theta}_{es}^* - \langle \theta_{e0} \rangle}{\tau_\theta} + \nabla \cdot \nu \nabla \theta_{e0}, \quad (10)$$

in which  $C_E \equiv C_{E*} (a + b |\mathbf{u}_0|)$  is the surface exchange coefficient for moist entropy,  $C_{E*}$  is an adjustable parameter, and  $\theta_{es}^*$  is the saturation EPT at the sea surface. The operator  $\langle \dots \rangle$  returns the domain average of the enclosed variable, and  $\bar{\theta}_{es}^*$  denotes the constant value of  $\langle \theta_{es}^* \rangle$ . The first two terms on the right-hand side of Eq. (10) are standard representations of what are usually the positive and negative moist-entropic interactions of the boundary layer with the sea surface and middle troposphere, respectively. The last term accounts for diffusion of  $\theta_{e0}$  by subgrid eddies. The third term supplements the explicit wind-induced

surface flux of moist entropy in driving  $\langle \theta_{e0} \rangle$  toward  $\bar{\theta}_{es}^*$ . Supplemental forcing is justifiable, because the reduced model ‘filters out’ fine-scale storm features, which are capable of producing strong wind fluctuations (gustiness). The forcing time-scale  $\tau_\theta$  is an adjustable parameter.

The middle-layer EPT is governed by an equation of the form

$$\partial_t \theta_{e1} + \mathbf{u}_1 \cdot \nabla \theta_{e1} = Q_{01}^c \frac{\theta_{e0} - \theta_{e1}}{h_1} + \frac{\bar{\theta}_{e1} - \langle \theta_{e1} \rangle}{\tau_\theta} + \frac{1}{h_1} \nabla \cdot \mathbf{v} h_1 \nabla \theta_{e1}. \quad (11)$$

The first term on the right-hand side tends to elevate moist entropy in the middle layer through shallow cumulus activity, whereas the last term accounts for diffusion of  $\theta_{e1}$  by subgrid eddy fluxes. The middle term slowly damps  $\langle \theta_{e1} \rangle$  toward the constant  $\bar{\theta}_{e1}$ , supposedly due to radiative cooling. The numerical model safeguards against excessively high values of middle-layer EPT by capping  $\theta_{e1}$  at  $\theta_{e2}^* - \delta\theta_{e1}$ , in which  $\delta\theta_{e1}$  is a small constant.

The saturation EPTs of the upper layer and sea surface are determined by the following linearized relations (O69):

$$\begin{aligned} \theta_{e2}^* &= \bar{\theta}_{e2}^* + \frac{\alpha}{c_{pd}} (\phi_2 - \phi_1), \\ \theta_{es}^* &= \bar{\theta}_{es}^* - \frac{\beta}{c_{pd}} \phi_1, \end{aligned} \quad (12)$$

in which  $\alpha$  and  $\beta$  are positive constants,  $c_{pd}$  is the isobaric specific heat of dry air, and  $\bar{\theta}_{es}^*$  was defined previously. The new constant  $\bar{\theta}_{e2}^*$  corresponds to the initial domain-average of  $\theta_{e2}^*$ . The top relation in Eq. (12) expresses the association of warming with expansion of the upper layer, since  $\phi_2 - \phi_1 = g(1 - \epsilon)(h_2 - H_2)$ . The bottom equation expresses the elevation of saturation entropy at lower values of the hydrostatic sea surface pressure, whose perturbation is given by  $p'_s = g\rho_0(h_1 + \epsilon h_2) - g\rho_0(H_1 + \epsilon H_2) \equiv \rho_0\phi_1$ .

Closure of the cumulus parametrization requires a formula for  $Q_-$  or  $Q_+$ . We consider the following three options:

### 3.3.1. Convergence-based (CB) closure

The first closure follows the seminal hurricane model of O69. The convective mass fluxes at the interface of the boundary layer and free troposphere are given by

$$\begin{aligned} Q_+ &= \max\{0, -H_0 \nabla \cdot \mathbf{u}_0\} \\ \text{and } Q_- &= \max\{0, H_0 \nabla \cdot \mathbf{u}_0\}. \end{aligned} \quad (13)$$

Equations (13) trivially satisfy constraint (9). In this closure, cumulus activity and low-level subsidence are confined to regions of boundary layer convergence and divergence, respectively. Convection may amplify convergence, but may not initiate convergence.

It is generally agreed that CB closure tends to let ‘Ekman pumping’ regulate convective updraughts. However, the primary RAMS simulation of section 2 suggests that surface friction has little influence on daily precipitation patterns during the intermediate stage of genesis (Figure 5). This motivates consideration of alternative closures.

### 3.3.2. Boundary layer quasi-equilibrium (BLQ) closure

The first alternative closure melds the convergence-based parametrization of O69 with the boundary layer quasi-equilibrium scheme of Zehnder (2001; cf. Raymond, 1995). With BLQ closure, strong winds can generate substantial convection where there is negligible pre-existing convergence, merely by enhancing the surface flux of moist entropy.

The derivation of BLQ closure begins by considering the prognostic equation for boundary layer EPT (Eq. (10)). Neglecting diffusion and minor supplemental forcing, the material derivative of  $\theta_{e0}$  vanishes as  $Q_-$  ( $Q_{10}^c$ ) approaches

$$C_E |\mathbf{u}_0| \frac{\theta_{es}^* - \theta_{e0}}{\theta_{e0} - \theta_{e1}} \equiv Q_-^e. \quad (14)$$

If convection acts to maintain entropic equilibrium in the boundary layer, then  $Q_-$  must be driven towards  $Q_-^e$  over some time-scale  $\tau_e$ . Accordingly, we may suppose that  $Q_- = Q_-^{qe}$ , in which the ‘quasi-equilibrium’ mass flux is governed by

$$\partial_t Q_-^{qe} + \mathbf{u}_0 \cdot \nabla Q_-^{qe} = \frac{Q_-^e - Q_-^{qe}}{\tau_e}. \quad (15)$$

But this solution is not entirely feasible. Local mass conservation in the boundary layer (Eq. (9)) requires that the upward cumulus mass flux obeys the following constraint:

$$Q_+ = Q_- - H_0 \nabla \cdot \mathbf{u}_0.$$

Therefore, a non-negative value of  $Q_+$  is possible only if  $Q_-$  equals or exceeds  $H_0$  times the local divergence. To ensure this condition, we let

$$Q_- = \max\{Q_-^{qe}, H_0 \nabla \cdot \mathbf{u}_0\}. \quad (16)$$

In addition, the numerical model caps  $Q_-^{qe}$  at an adjustable value  $W_e$ . Note that, if  $Q_-^{qe}$  is initially zero, then

$$\begin{aligned} Q_+ &= \max\{0, -H_0 \nabla \cdot \mathbf{u}_0\} \\ \text{and } Q_- &= \max\{0, H_0 \nabla \cdot \mathbf{u}_0\}, \end{aligned}$$

in the limit  $\tau_e \rightarrow \infty$ . That is, the model reduces to a classic convergence-based parametrization (O69). For small values of  $\tau_e$ ,  $Q_-^{qe}$  should be close to its equilibrium value  $Q_-^e$ . Weak convergence relative to  $Q_-^e/H_0$  would merely modulate the upward cumulus mass flux ( $Q_+$ ), but strong convergence would control it.

### 3.3.3. Selective boost (SB) closure

The third closure assumes that unresolved or neglected perturbations in the lower troposphere may stimulate cumulus activity where there is little convergence, but where relatively high convective instability exists between the boundary and middle layers. In other words, strong instability ‘selectively boosts’ convergence-based convection.

Moving on to equations, the mass flux out of the boundary layer is determined by

$$Q_+ = \max\left\{0, (Q_+^b - H_0 \nabla \cdot \mathbf{u}_0)\right\}, \quad (17)$$

in which  $Q_+^b$  represents the selective boost. In regions of weak convergence,  $Q_+^b$  may dominate the right-hand side. Given  $Q_+$ , the downward mass flux ( $Q_-$ ) is calculated directly from Eq. (9).

The selective boost of cumulus activity is governed by a prognostic equation of the form

$$\partial_t Q_+^b + \mathbf{u}_0 \cdot \nabla Q_+^b = \frac{Q_+^e - Q_+^b}{\tau_b}, \quad (18)$$

in which  $Q_+^e$  represents an equilibrium value obtained over a time-scale  $\tau_b$ . We assume that  $Q_+^e$  is non-zero only where the stability parameter  $S \equiv \theta_{e0} - \theta_{e1}^*$  exceeds a threshold value of  $S_{th}$ . One acceptable formula is given below

$$Q_+^e \equiv \begin{cases} W_b \left[ \frac{S_{th}(S - S_{th})}{10(\Delta S)^2} \right]^n, & S \geq S_{th}, \\ 0, & \text{otherwise,} \end{cases} \quad (19)$$

in which  $W_b$ ,  $\Delta S$  and  $n$  are positive constants. In order to evaluate  $S$ , we use the crude approximation  $\theta_{e1}^* = \theta_{e2}^*$ . Furthermore, we let

$$S_{th}(t) = \max\{0, (\max[S] - \Delta S)\}.$$

Clearly, we have made no effort to apply physical constraints in deriving the quantitative details of the SB closure. It is considered here only for qualitative comparison with the more commonly used CB and BLQ schemes. It is worth noting that the SB closure allows precipitation-cooled downdraughts ( $Q_-$ ) to locally quench deep convection (dramatically lower  $\theta_{e0}$  and  $\eta$ ) in regions of low  $\theta_{e1}$ . The possibility of local quenching is a distinct property of this closure. By contrast, the CB closure lowers  $\theta_{e0}$  through non-local clear-air subsidence. The BLQ closure includes local downdraughts, but these downdraughts merely act to balance the wind-induced surface flux of moist entropy.

### 3.4. Mass flux due to radiative cooling

Over time, cumulus convection tends to increase the average thickness ( $\langle h_2 \rangle$ ) of the upper layer, which corresponds to mean warming. To counter the warming, we uniformly relax the upper atmosphere toward its equilibrium thickness  $H_2$  over the time-scale  $\tau_h$ . This involves a downward mass flux at the interface between the middle and upper layers, given by

$$Q_{21}^r = \begin{cases} \frac{\langle h_2 \rangle - H_2}{\tau_h}, & \langle h_2 \rangle \geq H_2, \\ 0, & \text{otherwise.} \end{cases} \quad (20)$$

All other elements of the radiative mass flux matrix are zero.

### 3.5. Numerics

Discretization of the model for practical implementation is an important issue, but there is no attempt here to offer the best solution. Instead, this study uses a traditional finite-difference technique similar to that of SD09. The dynamical core is based on the potential-entropy-conserving shallow-water model of Sadourny (1979). A time-split algorithm is used to efficiently advance the flow while preventing numerical instabilities associated with fast gravity waves (cf. Skamarock and Klemp, 1992). The code is completely parallelized in the Message Passing Interface (MPI) paradigm, and is practical for use on a modern desktop workstation.

Table I. Parameters of the reduced model for simulations over a cool ocean.

	Values
Common parameters	
$D, d$	2000, 3.906 (km)
$H_0, H_1, H_2$	1, 5, 5 (km)
$\epsilon, \alpha, \beta$	0.9, 9.5, 2.0
$\bar{\theta}_{e1}^*, \bar{\theta}_{e1}, \bar{\theta}_{e2}^*, \delta\theta_{e1}$	352.3, 323, 328, 0.25 (K)
$\tau_h, \tau_\theta$	6 (h), 5 (days)
$\mu, \xi$	$5.0 \times 10^{-4}$ ( $\text{m s}^{-1}$ ), 0.025
$\eta, \eta_u, \lambda$	0, 35, 0.25
$g$	9.80665 ( $\text{m s}^{-2}$ )
$c_{pd}$	1005.7 ( $\text{J kg}^{-1} \text{K}^{-1}$ )
$C_{D*}, C_{E*}$	1, 1 (unless stated otherwise)
BLQ closure parameters	
$\tau_e, W_e$	6 (h), 0.5 ( $\text{m s}^{-1}$ )
SB closure parameters	
$\tau_b, W_b, \Delta S, n$	6 (h), 0.5 ( $\text{m s}^{-1}$ ), 1 (K), 2

## 4. Comparison of tropical cyclogenesis in the reduced model and RAMS

The following compares tropical cyclogenesis in RAMS to the reduced model. All three cumulus parametrizations of the reduced model are considered. These include parametrizations with convergence-based (CB), boundary layer quasi-equilibrium (BLQ) and selective boost (SB) closures. The reader may consult section 3.3 for brief descriptions of each.

### 4.1. Initialization and settings of the reduced model for genesis over a cool ocean

Our comparison will focus on hurricane formation over a cool ocean at  $10^\circ\text{N}$ . The initial conditions of the reduced model correspond to the RAMS simulation at  $t = 4.33$  days, at which point the rotational convective turbulence has developed quasi-stationary spectral characteristics (see section 4.6). Figures 2 (top row, second panel) and 5 illustrate the lower-tropospheric vorticity and moist convection at this time. The dominant storm activity happens to be concentrated in three distinct regions.

As in the RAMS simulation, the domain size  $D$  and grid spacing  $d$  are 2000 km and 3.9 km, respectively. The local values of  $\mathbf{u}_0$  and  $\theta_{e0}$  in the reduced model are mass-weighted vertical averages of the horizontal velocity and EPT in the lowest 1 km of the RAMS simulation. Equation (C2) of Appendix C provides the working definition of EPT. The local values of  $\mathbf{u}_1$  and  $\mathbf{u}_2$  are taken along pressure isosurfaces at 700 and 300 hPa, respectively. The local values of  $\theta_{e1}$  are taken along the pressure isosurface at 700 hPa. The mass fields ( $h_1$  and  $h_2$ ) are initialized to ‘balance’ the vorticity fields in the middle and upper layers, as explained in Appendix B. Furthermore,  $Q_+^{qc}$  and  $Q_+^b$  are initialized to zero in the BLQ and SB cumulus parametrizations.

Table I summarizes the constant parameters of the reduced model. The values of  $H_m$ ,  $\epsilon$ ,  $\alpha$ ,  $\beta$ ,  $\mu$ ,  $g$  and  $c_{pd}$  are equal (or nearly equal) to those of O69 and SD09. The values of  $\bar{\theta}_{e1}$  and  $\bar{\theta}_{e2}^*$  are marginally consistent with the domain averages of the RAMS simulation between days 3

and 10 of genesis, with  $\bar{\theta}_{e1}$  slightly elevated to prevent excessive decay of  $\theta_{e0}$  by downdraughts. The value of  $\bar{\theta}_{es}^*$  corresponds to a sea-surface temperature of 26°C and a surface pressure of 1015.1 hPa. The parameters  $\eta_l$  and  $\eta_u$  are the lower and upper limits of  $\eta$  imposed by the numerical model. They replace Eq. (7) when the right-hand side is out of bounds. A lower bound of  $\eta_l = 0$  is required because a negative value of  $\eta$  is nonsensical. A finite upper bound ( $\eta_u$ ) is required to safeguard against numerical instability under extraordinary circumstances. The detrainment parameter is relatively large in order to enhance mid-level moistening, but still satisfies the constraint  $\lambda \ll 1$ .

A value of 6 h for  $\tau_h$  may seem short for domain-scale radiative cooling. However, much larger values of  $\tau_h$  lead to excessive warming, slower genesis, and weakening of the steady-state hurricane in the reduced model. It is reasonable to propose that  $\tau_\theta$  and  $\tau_h$  should have the same order of magnitude, but here we let  $\tau_\theta = 5$  days. With this setting, the domain averages of  $\theta_{e0}$  and  $\theta_{e1}$  stay fairly consistent with the RAMS simulation during tropical cyclogenesis.

The value of  $W_e$  is such that convergence of  $\mathbf{u}_0$  much greater than  $0.5 \times 10^{-3} \text{ s}^{-1}$  necessarily provides the dominant updraught in the BLQ parametrization. The author has verified that increasing  $W_e$  by a factor of 20 hardly affects genesis in the primary BLQ simulation, for which  $C_{E*} = C_{D*} = 1$ . Letting  $W_b = W_e$  in the SB parametrization provides some degree of consistency.

#### 4.2. Qualitative pathway of hurricane formation

Figure 7 illustrates the evolution of wind speed, relative vorticity and deep convection in the reduced model with BLQ closure. The CB and SB closures produce similar images. Rather than coalesce as in RAMS (Figure 2 (top)), the three initial regions of concentrated storm activity (elevated vorticity) separately produce tropical cyclones, of either hurricane or tropical storm strength. The basic pathway to genesis in each region resembles that described more fully in SD09. During the unshown transition to day 9, local positive vorticity anomalies merge and axisymmetrize, as would occur in ordinary 2D turbulence (Melander *et al.*, 1987, 1988; Carnevale *et al.*, 1991; Dritschel and Waugh, 1992; Lansky *et al.*, 1997; Schechter and Dubin, 1999, 2001; Schubert *et al.*, 1999; Schechter *et al.*, 2000; Möller and Montgomery, 2000; Schechter and Montgomery, 2003). As the first incipient tropical cyclone begins to intensify, an asymmetric eyewall with mesovortices forms near the radius of maximum wind. As intensification continues, the eyewall contracts (cf. SW82; Schubert and Hack, 1982 (SH82)). Eventually, the vortex settles into a metastable warm-core equilibrium with a discernible eye and outer precipitation bands. After a longer time, the tropical cyclones originating from separate regions spontaneously merge into one.

Figure 8(a) shows the domain maximum of  $|\mathbf{u}_0|$  versus time in the reduced model. Each curve corresponds to a distinct cumulus parametrization, with  $C_{D*}$  equal to 1 or 0. The onset of rapid intensification begins at about day 9 for the control (frictional) simulations with BLQ and SB closures. The CB closure slightly accelerates genesis, possibly because it neglects the stabilizing influence of precipitation cooled downdraughts. All control simulations suggest that interaction with neighbouring vortices limits the intensity of a tropical cyclone. Maximal intensity is achieved only after

the vortices merge. The simulations without surface drag are discussed in section 4.3.

During the intermediate stage of genesis, two qualitative features of convection in RAMS are distinguishable from the reduced model with any cumulus parametrization:

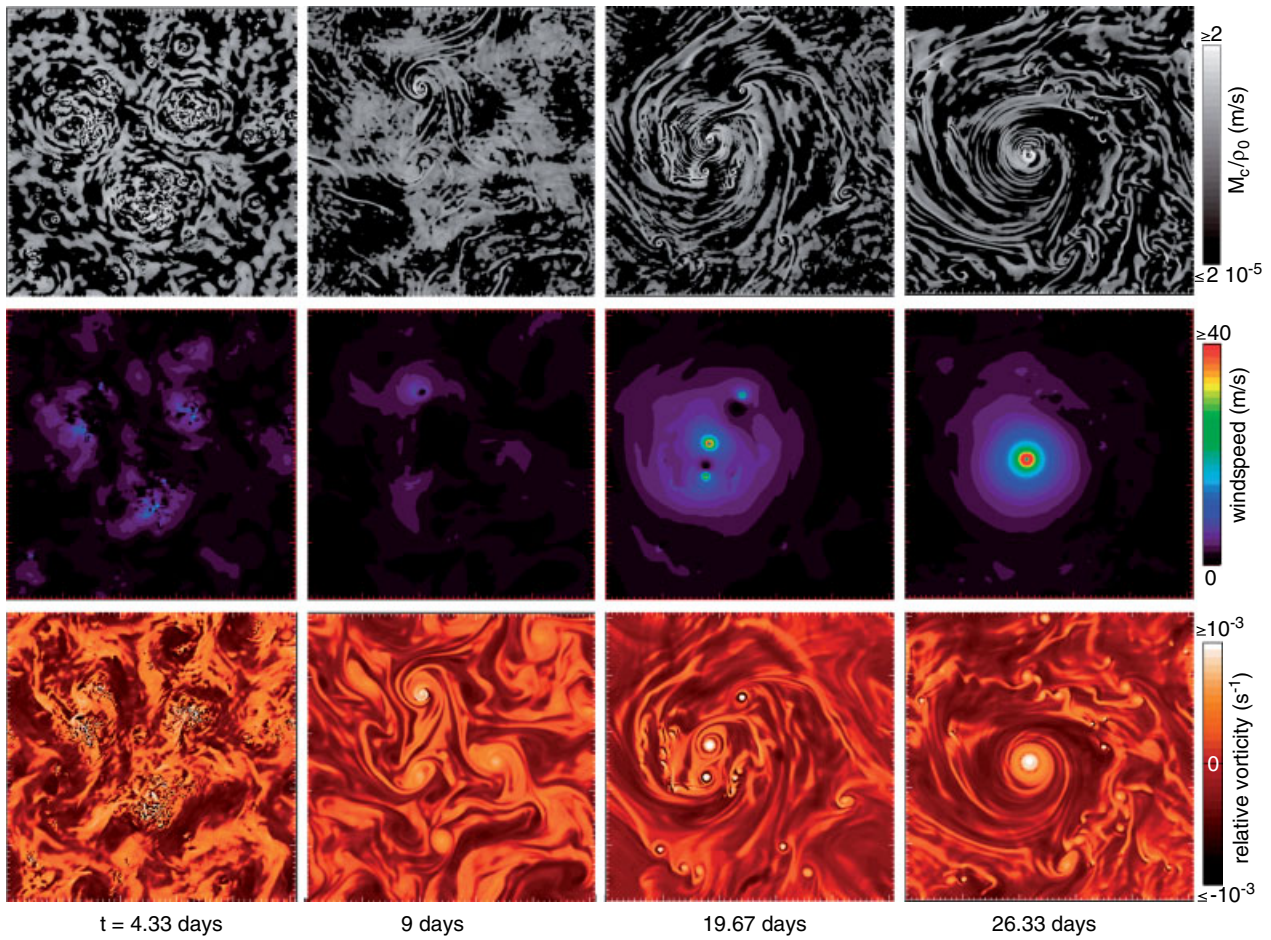
- (i) storms in RAMS are comparatively sporadic;
- (ii) strong wind fluctuations in RAMS persistently appear at minimally resolved scales, from the boundary layer to the upper troposphere. Both (i) and (ii) seem consistent with direct modelling of cloud processes, and are relevant to the pathway of genesis. Sporadic convection in RAMS (item (i)) occasionally creates new mesocyclones that dominate their predecessors and reconfigure the flow pattern. By contrast, a few coherent mesocyclones emerge early on in the reduced model, and persist. These primary mesocyclones have relatively little interference building up moist entropy in the lower and middle troposphere, which theoretically and empirically facilitates tropical cyclogenesis (e.g. Emanuel, 1991). It is therefore reasonable that the reduced model produces more tropical cyclones. On the other hand, the cumulus parametrizations of the reduced model fail to regenerate strong wind fluctuations (item (ii)) after their initial dissipation at small scales. Consequently, the domain maximum wind speed in Figure 8(a) decays considerably at the beginning of the simulation. Reduction of gustiness reduces moist entropy production, which adversely affects genesis. Such artificial reduction was used to justify minor supplemental forcing of  $\theta_{e0}$  in Eq. (10) of the reduced model.

#### 4.3. Variation of $C_D$ , $C_E$ and the SST

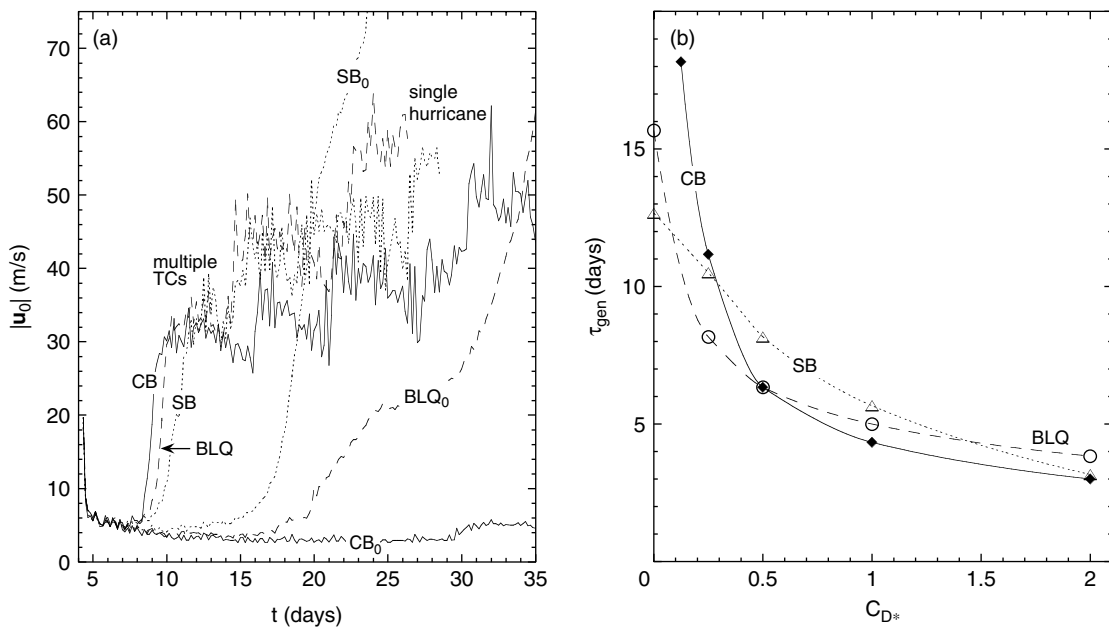
Figure 8(a) demonstrates that removing surface drag from the reduced model generally hinders tropical cyclogenesis, as in RAMS. With CB closure, no hurricane develops. This result is unsurprising, given that CB closure theoretically requires Ekman-like pumping to stimulate the intensification of a cyclone, in which deep conditional instability ( $\theta_{e0} > \theta_{e2}^*$ ) is sustained by wind-induced surface fluxes of moist entropy (O69; SD09). With BLQ or SB closure, surface entropy fluxes do not require assistance from Ekman-like pumping to coherently ‘force’ enhanced levels of deep convection in the vortex core. Therefore, despite slowing down the process, removing surface drag does not prevent hurricane formation in the BLQ or SB version of the reduced model.

Figure 8(a) does not show the equilibration amplitudes of the frictionless BLQ and SB hurricanes. Basic steady-state theory would predict an implausibly strong hurricane, if (improperly) extrapolated toward  $C_{D*} = 0$  (S10; E86). In practice, the central pressure deficit decreases over time until the local value of  $h_1$  becomes zero, at which point the model is nonsensical and the numerics breakdown. In other words, a so-called ‘hypercanine instability’ occurs.

Figure 8(b) shows a measure of the tropical cyclogenesis time-scale ( $\tau_{\text{gen}}$ ) versus  $C_{D*}$  for all three cumulus parametrizations. For these simulations,  $\tau_{\text{gen}}$  is conveniently equated to the time ( $t - 4.33$  days) at which the maximum of  $|\mathbf{u}_0|$  surpasses  $10 \text{ m s}^{-1}$ , following the onset of intensification (cf. SD09). The CB curve for  $\tau_{\text{gen}}$  does not dramatically diverge from the BLQ or SB curves until  $C_{D*}$  becomes much less than unity. Conceivably, fine tuning of the BLQ or SB closure could reduce the growth of  $\tau_{\text{gen}}$  as  $C_{D*} \rightarrow 0$ , but this would not be desirable if the goal is to better resemble the behaviour of RAMS. Note that increasing  $C_{D*}$  above an



**Figure 7.** (Top row) The cumulus mass flux  $M_c$  into the upper layer, (middle row) the boundary layer wind speed  $|u_0|$ , and (bottom row) the relative vorticity  $\zeta_1$  of the middle layer during tropical cyclogenesis in the reduced model with BLQ closure. The grey scale for  $M_c$  is logarithmic, whereas the colour scale for  $|u_0|$  is linear. The colour scale for  $\zeta_1$  is identical to that in Figure 2. Each panel shows the entire  $2000 \times 2000$  km horizontal domain.



**Figure 8.** (a) Time series of the maximum boundary layer wind speed in the reduced model with convergence-based (CB), boundary layer quasi-equilibrium (BLQ) and selective boost (SB) cumulus parametrizations. A blank or zero subscript on the curve label indicates a simulation with  $C_{D*} = 1$  or  $C_{D*} = 0$ , respectively. All simulations except  $CB_0$  produce hurricanes. (b) Drag dependence of the genesis time-scale ( $\tau_{gen}$ ) in the reduced model with CB, BLQ and SB closures. In all cases,  $C_{E*} = 1$ .

unrealistically large threshold (not shown) would prevent genesis, regardless of the cumulus parametrization. The reason seems clear: vortex intensity theoretically vanishes with the ratio  $C_{E^*}/C_{D^*}$ , due to insurmountable dissipation (S10; E86).

For brevity, we will not thoroughly discuss the variation of  $\tau_{\text{gen}}$  with  $C_{E^*}$  or the SST. The author has verified that setting  $C_{E^*}$  to zero invariably suppresses hurricane formation in the reduced model (cf. O69; SD09). Using CB closure, SD09 previously showed that tropical cyclogenesis monotonically accelerates as  $C_{E^*}$  increases from zero to a realistic value. SD09 also showed that tropical cyclogenesis accelerates with increasing SST, as in RAMS.

#### 4.4. The relevance of $\eta$ for rapid intensification

A comprehensive review of competing theories for the intensification of an incipient tropical storm is beyond the scope of this paper. Those interested in the historical development of the subject may readily consult the literature (Eliassen, 1952; Charney and Eliassen, 1964; O69; Ooyama, 1982; SW82; SH82; HS86; RE87; Emanuel, 1989 (E89); GC98; Smith, 2000; KD03; Smith *et al.*, 2005, 2009; Raymond *et al.*, 2007; Kieu and Zhang, 2009; Marin *et al.*, 2009; Tory and Frank, 2010). The earliest theories based on the reduced model emphasize that  $\eta$  (a combined measure of deep convective instability and middle-tropospheric moisture defined by Eq. (7)) must exceed a critical value in the main updraught region to facilitate spin up. The same theories suggest that intensification accelerates with increasing  $\eta$ , *all else being equal*. A more recent line of thought emphasizes that the cyclone may readily adjust from one state of (slantwise) convective neutrality to a stronger state, in response to changes of the moist entropy (EPT) distribution in the boundary layer (E89; GC98). From this perspective, there is no direct connection between  $\eta$  and the intensification rate. Still, an abnormal elevation of  $\eta$  in the core of the vortex could provide some indication of adequate preconditioning for the initiation of intensification into a hurricane.

Figure 9 shows the time series of the average value of  $\eta$  in areas of strong convection, for the reduced simulations of tropical cyclogenesis whose parameters are given by Table I. Here, the average value of  $\eta$  is defined by

$$\langle \eta \rangle_+ \equiv \frac{\int d^2\mathbf{x} Q_+^3 \eta}{\int d^2\mathbf{x} Q_+^3}, \quad (21)$$

in which the integrals are over the entire horizontal domain. The weight factor  $Q_+^3$  effectively constrains the integrand to the main updraught regions of developing storms. The time series of the domain-maximum wind speed (in the boundary layer) is superposed on each plot for reference. Only the first intensification event is shown.

For all three cumulus parametrizations, the onset of rapid intensification coincides with pronounced growth of  $\eta$ . In the CB and BLQ simulations, the prominent spikes of  $\eta$  are connected to substantial elevations of EPT in both the lower and middle layers of the incipient tropical storm. In the SB simulation, the spike primarily results from a rapid increase of  $\theta_{e1}$ . As the upper troposphere warms within the vortex core,  $\eta$  drops toward  $1/(1-\lambda)$ , which corresponds

to zero net entrainment of air from the middle layer by cumulus updraughts (in the reduced model). Zero net entrainment inhibits convergence of angular momentum in the middle layer, and halts rapid intensification. Since  $\lambda \ll 1$ , the arrest of intensification coincides with the establishment of quasi-neutrality to deep convection, in which  $\theta_{e0} \approx \theta_{e2}^*$ .

Figure 10(a) is a plot of  $\eta$  for the RAMS simulation. The plotted values of  $\eta$  are spatial averages defined by

$$\langle \eta \rangle_+ \equiv \frac{\int_s d^2\mathbf{x} W \eta}{\int_s d^2\mathbf{x} W}, \quad (22)$$

in which the integral  $\int_s$  covers a  $437.5 \times 437.5$  km square near the centre of the domain. The weight factor  $W$  is either the vertical velocity  $w$  at  $z = 1$  km, the squared relative vorticity  $\zeta^2$  of the boundary layer, or the column-integrated rain mass  $P_c$ . In the former two cases,  $W$  is set to zero where either  $w$  or  $\zeta$  is negative. The time series for  $\eta$  is qualitatively insensitive to the choice of  $W$ , or to a larger integration domain. The definitions of  $\theta_{e0}$  and  $\theta_{e2}^*$  used to evaluate  $\eta$  (Eq. (7)) in the RAMS simulation are equivalent to those of section 4.1, but  $\theta_{e1}$  is evaluated at 600 hPa. If  $\eta$  is less than 0 or greater than 35, it is reset to 0 or 35, as in the reduced model. Furthermore, all field variables are smoothed onto a quarter-resolution grid prior to evaluation.

In the RAMS simulation, the time-series of  $\eta$  consists of quasi-periodic oscillations superposed on a basic trend that peaks near the onset of rapid intensification, as in the reduced model. The secondary  $\eta$  oscillations are closely related to convective cycles. Figure 10(b) illustrates the convective state during a typical trough, and during the distinguished peak at which an incipient hurricane bursts into action. A trough in  $\eta$  corresponds to a state with numerous convectively active regions that have lowered the entropy of the boundary layer (as by generating precipitation-cooled downdraughts) and reduced local CAPE. As convection subsides following a trough, surface fluxes of sensible and latent heat help restore CAPE and  $\eta$ . Such restoration creates favourable conditions for renewed cumulus activity.<sup>§</sup>

The reason why hurricane formation does not rapidly ensue after an earlier secondary peak of  $\eta$  is not entirely clear, and will remain a topic of future research. Many inhibitors are possible, including horizontal strain and vertical windshear acting on the mesoscale cyclones. Interestingly, the pseudo-kurtosis of boundary layer relative vorticity, here defined by

$$K_\zeta \equiv \sqrt{\frac{\int_s d^2\mathbf{x} \zeta_0^4 / \int_s d^2\mathbf{x}}{(\int_s d^2\mathbf{x} \zeta_0^2 / \int_s d^2\mathbf{x})^2}}, \quad (23)$$

spikes simultaneously with  $\eta$  at the onset of rapid intensification (Figure 10). This may reflect the development of a robust vortex core before dramatic acceleration of the wind speed. An increase of inertial stability within the core might also facilitate further intensification, by enabling a more efficient response to latent heat release (SH82; HS86).<sup>¶</sup>

<sup>§</sup>The secondary oscillations of  $\eta$  may be sensitive to the domain size of the RAMS simulation (cf. Nolan, 2007), but this matter is not investigated here.

<sup>¶</sup>In the reduced model,  $K_\zeta$  tends to increase more gradually during intensification.

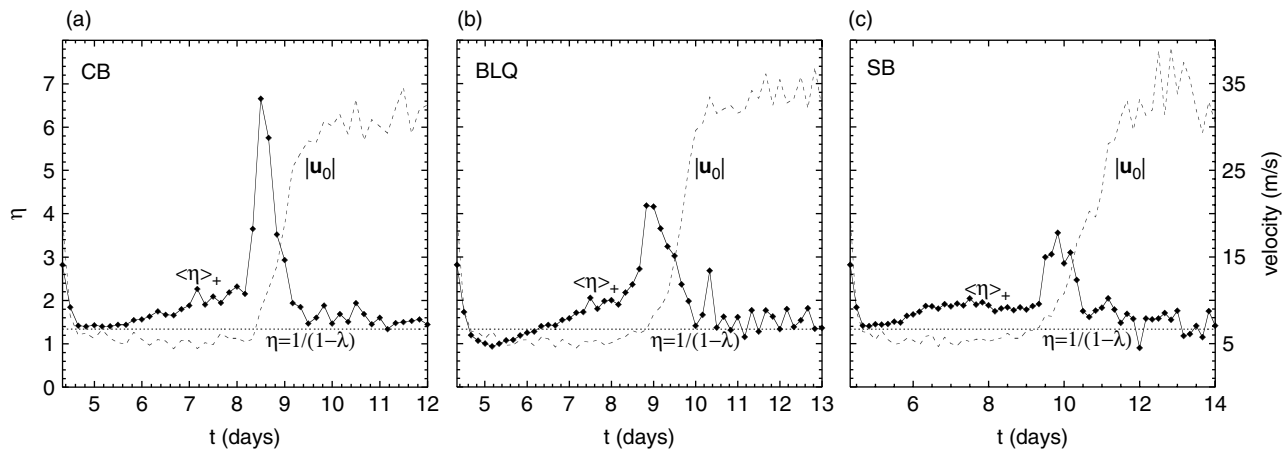


**Figure 9.** Time series of  $\eta$  (solid curve with diamonds) in convectively active regions during tropical cyclogenesis in the reduced model from simulations with (a) CB, (b) BLQ and (c) SB closures. The dashed curve in each plot shows the maximum wind speed in the boundary layer.

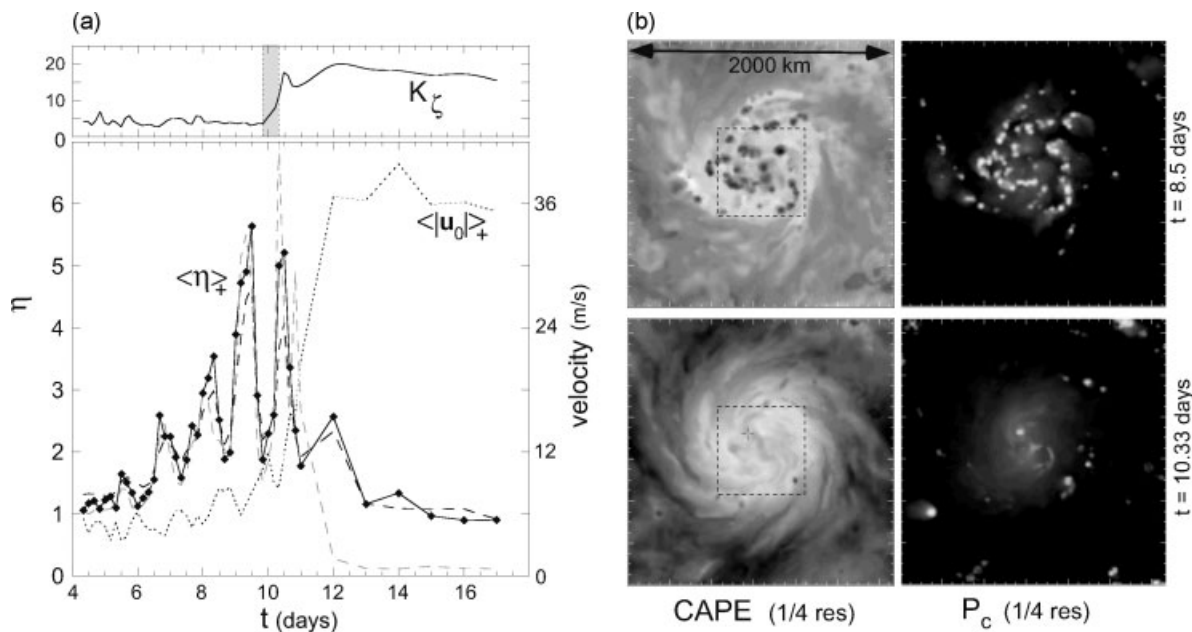


**Figure 10.** (a) Time series of  $\eta$  during tropical cyclogenesis in RAMS. The solid (with diamonds), dark-dashed and light-dashed curves respectively correspond to averages weighted by  $P_c$ ,  $w_{1\text{km}}$  and  $\zeta_0^2$ , as explained in section 4.4. The dark-dotted curve shows the average horizontal wind speed, with  $P_c$  weighting, in the boundary layer. The top graph shows the pseudo-kurtosis of relative vorticity in the boundary layer ( $K_\zeta$ ); the shaded region spans from trough to peak of the secondary  $\eta$  oscillation that immediately precedes the dramatic wind speed acceleration. (b) Snapshots of CAPE and column-integrated rain mass ( $P_c$ ) on the quarter-resolution grids on which all field variables are here calculated, before (top row) and at the onset (bottom row) of rapid intensification. The grey scale is linear for CAPE and logarithmic for  $P_c$ . White corresponds to the maximum (over both snapshots) of the plotted field variable; black corresponds to zero CAPE, or values less than  $10^{-4}$  times the maximum  $P_c$ . The cross (+) on the lower left plot marks the location of the core of the incipient hurricane. The dashed squares contain the averaging domain of the  $\langle \dots \rangle_+$  operator.

The decay of  $\eta$  toward unity (or less) during rapid intensification in RAMS compares favourably to the reduced model, and is consistent with a transition to approximate slantwise convective neutrality. Taking into consideration both Figures 10 and C1 (Appendix), the vortex does not appear to be quasi-neutral while it intensifies. The same is true in the reduced model, where quasi-neutrality would imply  $\eta \approx 1$  throughout the process. Of course, one should not leave with the impression that intensification is merely the partial conversion of initial CAPE (or slantwise CAPE) into tangential wind. As mentioned earlier, a non-zero surface flux of moist entropy (finite  $C_E$ ) is required to sustain intensification in either model.

#### 4.5. The mature storm

Let us now briefly divert our attention from hurricane formation to steady-state structure. An informal theory for steady-state intensity in the reduced model has been developed and verified elsewhere (S10). As in the more realistic but involved theory of E86, the square of the maximum tangential wind speed is roughly proportional to the ratio of entropy to momentum exchange coefficients, times a measure of the ambient thermal disequilibrium between the sea surface and the upper troposphere. Basic agreement with E86 is not accidental; however, some details of steady-state structure in the reduced model may differ from those of a realistic hurricane. The following illustrates

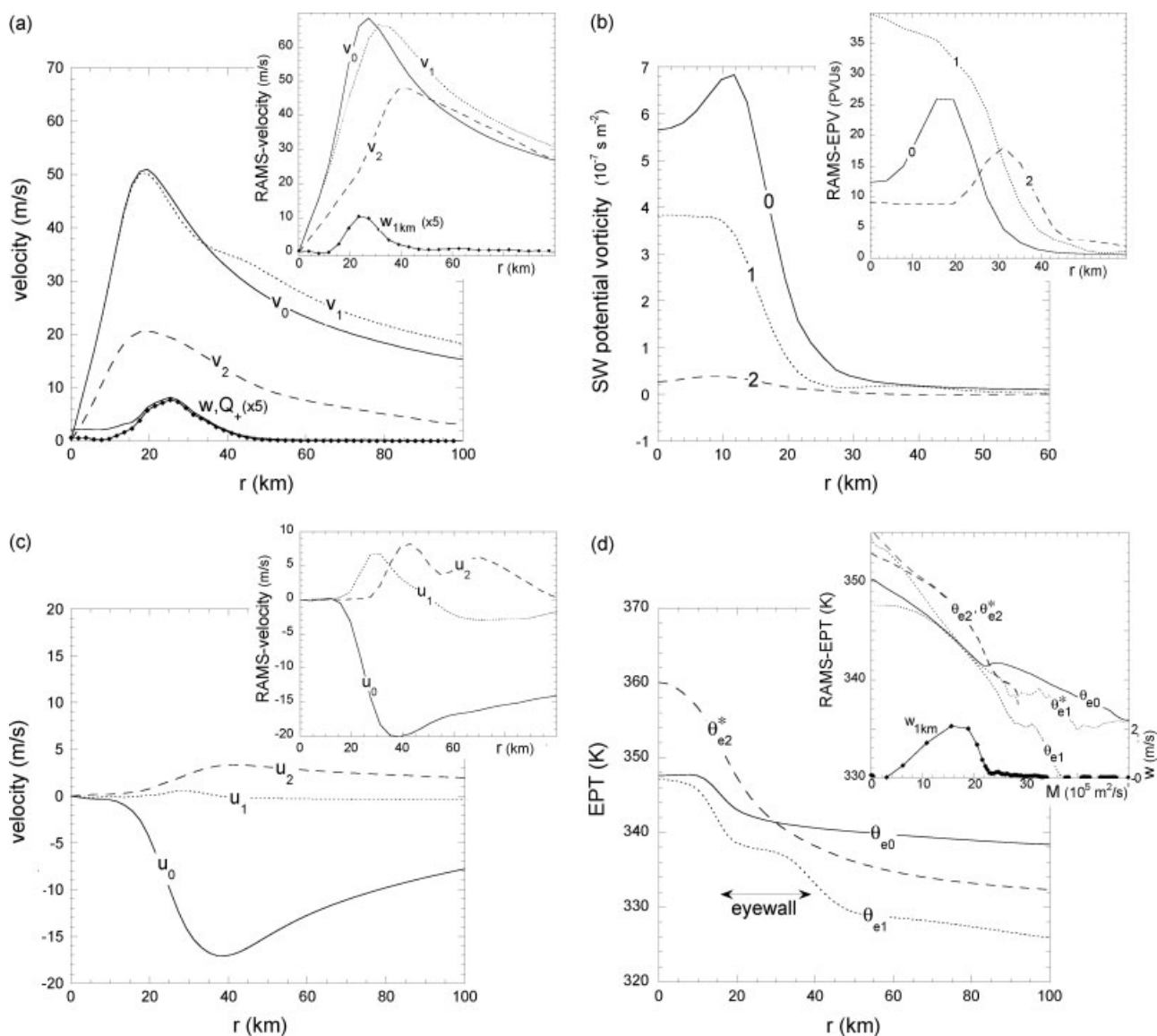


**Figure 11.** Mature hurricane in the reduced model with BLQ closure, compared to its counterpart in RAMS (insets). All fields of the reduced hurricane are averaged over azimuth and a 32 h time period. All fields of the RAMS hurricane are azimuthal averages at  $t = 16$  days. (a) Tangential velocity, vertical velocity ( $w \equiv Q_+ - Q_-$ , diamonds) and the upward cumulus mass flux ( $Q_+$ ) at the top of the boundary layer. The variable  $w_{1km}$  (inset) is the vertical velocity of the RAMS hurricane 1 km above the surface. (b) Potential vorticity. The shallow-water (SW) potential vorticity of the reduced hurricane is  $(\zeta_l + f)/gh_l$ , whereas the Ertel potential vorticity (EPV) of the RAMS hurricane is  $(\zeta + f\hat{z}) \cdot (\nabla_{3D}\theta)/\rho$ , in which  $\theta$  is the ordinary potential temperature. (c) Radial velocity. (d) Equivalent potential temperature (EPT) and saturation EPT. For the RAMS hurricane, the radial coordinate  $r$  is replaced by the absolute angular momentum  $M$ . In all plots, the labels 0, 1 and 2 correspond to the boundary layer, middle layer (700 hPa in RAMS) and upper layer (300 hPa in RAMS), respectively.

the adequacies and shortcomings of mature hurricane structure in the reduced model.

Figure 11 shows the basic state of the final hurricane that forms after three tropical cyclones merge in the BLQ simulation. All fields are azimuthal means, averaged over a 32 h time period beginning at  $t = 26.33$  days. To improve accuracy, the spatial resolution of the reduced model was refined from 3.9 to 2 km during the averaging interval. For comparison, the insets show the azimuthally averaged state of the RAMS hurricane at  $t = 16$  days. Details of the radial profiles may vary with the precise centring of the cylindrical coordinate system, but the results shown here seem reasonable. For the reduced model, the central axis of the cylindrical coordinate system intersects the minimum of the stream function associated with the rotational (vortical) component of the boundary layer flow field. For the RAMS

simulation, the central axis intersects the point of minimum surface pressure.<sup>||</sup>

Figure 11(a) plots the radial profile of the azimuthal wind speed  $v$  of each layer. Lower wind speed in the upper troposphere is characteristic of a warm-core cyclone in gradient balance. The radius of maximum wind speed ( $r_{mw}$ ) is about 20 km, compared to 27 km in RAMS. The maximum wind speed itself is  $51 \text{ m s}^{-1}$ , compared to  $68 \text{ m s}^{-1}$  in RAMS. Weaker winds do not indicate a critical defect, since fine tuning of the secondary model parameters (such as  $\alpha$ ) can strengthen the reduced hurricane (S10). Similar fine tuning might also reduce the exaggerated baroclinicity. In addition to illustrating the primary circulation, Figure 11(a) shows

<sup>||</sup>Neither centring scheme used here is robust for weak or highly asymmetric hurricanes.

the vertical mass flow in the eyewall updraught, just above the boundary layer. Unlike the RAMS hurricane, the peak updraught velocity at this height ( $z = 1$  km) occurs at a radius greater than  $r_{mw}$ .

Figure 11(b) shows that the radial distribution of shallow-water potential vorticity (PV) in the reduced hurricane somewhat resembles the radial distribution of Ertel PV in the RAMS hurricane. The middle-layer PV decays monotonically with increasing radius  $r$ , whereas the boundary layer PV possesses an off-centre peak. The upper layer PV profile is non-monotonic, but the off-centre peak is much wider than its counterpart in RAMS. Figure 11(c) verifies that the secondary circulation consists of radial inflow in the boundary layer and outflow aloft. One distinguishing feature of the RAMS hurricane is pronounced mid-level outflow, associated with slantwise convection.

Figure 11(d) verifies that the lower-tropospheric EPT and upper-tropospheric saturation EPT of the reduced hurricane decay with increasing  $r$ .\*\* The inset plots select EPTs and saturation EPTs of the RAMS hurricane versus absolute angular momentum  $M$  (defined by Eq. (C1)). As Appendix C illustrates in greater detail, the eyewall of the RAMS hurricane exhibits approximate slantwise convective neutrality ( $\theta_e \approx \theta_e^*$  and  $\partial_z \theta_e^*|_M \approx 0$ ), although its upper-tropospheric section seems to have some degree of stability. By analogy, the eyewall of the reduced hurricane is quasi-neutral to deep vertical convection, in that  $\theta_{e0} \approx \theta_{e2}^*$ . Relatively low  $\theta_{e1}$  is considered a minor defect of the reduced model that is correctable by fine tuning of secondary parameters.

#### 4.6. Spectral characteristics of the horizontal flow during the intermediate stage of genesis

Section 4.2 addressed qualitative differences between the self-regulated convective forcing (and dissipation) of the reduced model and RAMS. Such differences are expected to cause quantitative discrepancies in the spectral distributions of horizontal kinetic energy, relative vorticity and horizontal divergence. Spectral discrepancies may also reflect incorrect mechanisms of mode-to-mode energy transfer in the reduced model. The purpose of this subsection is merely to compare the spectral distributions in RAMS and the reduced model. Rigorous theoretical discussion is left for a future time.

Figures 12(a, b and c) compare the spectral distributions of horizontal kinetic energy before tropical cyclones emerge in RAMS or the reduced model. The spectral energy density (power spectrum) is here defined by

$$dk \mathcal{E}_h(k + dk/2) \equiv \int_{0 \leq k' - k \leq dk} d^2 \mathbf{k}' \frac{\mathbf{U}_{\mathbf{k}'} \cdot \mathbf{U}_{\mathbf{k}'}^*}{2}, \quad (24)$$

in which  $\mathbf{k}$  is the horizontal wave number,  $k$  is the magnitude of  $\mathbf{k}$ ,  $\mathbf{U}_{\mathbf{k}}$  is the 2D Fourier transform of the horizontal velocity,  $\mathbf{U}_{\mathbf{k}}^*$  is the complex conjugate of  $\mathbf{U}_{\mathbf{k}}$ , and the integral is over an annulus of width  $dk$  in  $\mathbf{k}'$ -space centred at  $k' = k + dk/2$ .

The three plots of  $\mathcal{E}_h$  in the figure correspond to velocity fields of the boundary layer, middle troposphere and upper

troposphere. For the RAMS simulation, the middle- and upper-tropospheric velocity fields are taken on the 700 hPa and 300 hPa pressure isosurfaces, respectively; the boundary layer velocity field is a mass-weighted vertical average up to 1 km from the sea surface. The dashed curve in each plot is the common power spectrum of RAMS and the reduced model at  $t = 4.33$  days. By  $t = 7$  days, the RAMS simulation (solid curve) shows an increase of horizontal kinetic energy at the domain scale in the lower to middle troposphere, possibly due to vortex mergers. On the other hand, the spectral density remains unchanged at intermediate scales, where  $\mathcal{E}_h$  varies roughly as  $k^{-2}$ .

The dotted curves correspond to the reduced model runs at  $t = 7$  days. All three cumulus parametrizations yield approximately the same result. In the lower to middle troposphere,  $\mathcal{E}_h$  varies roughly as  $k^{-3}$  over the intermediate mesoscale. This relatively steep spectrum is reminiscent of freely evolving 2D turbulence (Danilov and Gurarie, 2000). The contrast with RAMS seems reasonable, in part because the cumulus parametrizations of the reduced model do not persistently generate energetic, small-scale storm features. In the upper layer, the kinetic energy appears to suffer significant broadband dissipation following initialization. One important cause is ‘cumulus friction’ (which conserves momentum but not kinetic energy). Another contributing factor is conversion of kinetic to potential energy.

Figures 12(d, e and f) show the spectral distributions (on day 7) of relative vorticity  $\zeta$  and divergence  $\sigma$  of the horizontal flow, defined by

$$dk \mathcal{Z}(k + dk/2) \equiv \int_{0 \leq k' - k \leq dk} d^2 \mathbf{k}' \zeta_{\mathbf{k}'} \zeta_{\mathbf{k}'}^*, \quad (25)$$

$$\text{and } dk \mathcal{D}(k + dk/2) \equiv \int_{0 \leq k' - k \leq dk} d^2 \mathbf{k}' \sigma_{\mathbf{k}'} \sigma_{\mathbf{k}'}^*,$$

respectively. In RAMS,  $\mathcal{D}$  consistently exceeds  $\mathcal{Z}$  (in the lower to middle troposphere) for wavelengths  $\Lambda \equiv 2\pi/k$  less than roughly 200 km. Substantial divergence in the intermediate (and small) mesoscale suggests the presence of considerable vortex stretching or inertia-gravity waves. In the reduced model, the spectral density of vorticity generally exceeds that of divergence until  $\Lambda$  falls below 50 km or less, depending on the altitude. In this sense, pre-hurricane turbulence in the reduced model resembles classic 2D turbulence down to much smaller scales.

We may firmly conclude that the boundary layers of RAMS and the reduced model have distinct spectral characteristics. However, vertical averaging of  $\mathbf{u}$  in the middle and upper troposphere of the RAMS simulation could yield better agreement with the reduced model. Appendix D briefly examines this issue. We find that  $\mathcal{E}_h$  in RAMS remains relatively high for  $\Lambda$  less than about 100 km. On the other hand, vertical averaging of  $\mathbf{u}$  (in the middle and upper troposphere) brings  $\mathcal{D}$  below  $\mathcal{Z}$  in the intermediate mesoscale. Therefore, vorticity dominance of the reduced model is not entirely inconsistent with RAMS above the boundary layer.

#### 4.7. Autocorrelation of strong vorticity anomalies in the boundary layer

The characteristic rate of change of strong vorticity anomalies in the boundary layer (or any other layer)

\*\*Setting  $\lambda = 0$  in the cumulus parametrization of the reduced model would prevent mid-level moistening and cause an artificial EPT deficit in the lower tropospheric layers of the eye (SD09).

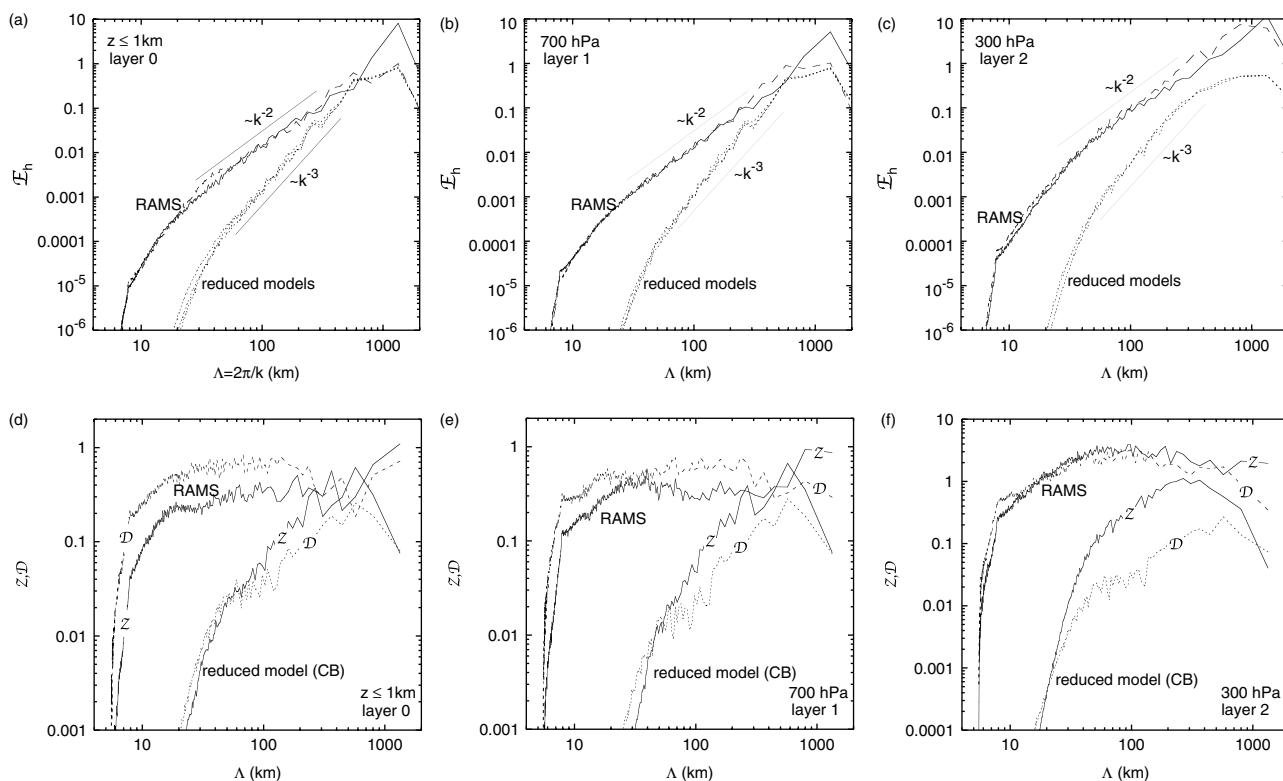


**Figure 12.** (Top row) The horizontal kinetic energy spectrum  $\mathcal{E}_h$  in the (a) lower, (b) middle and (c) upper troposphere on day 7 of tropical cyclogenesis. The solid curve corresponds to the RAMS simulation and the dotted curves correspond to the reduced model with CB, BLQ and SB closures. For reference, the dashed curve in each plot shows the common spectrum of all simulations at  $t = 4.33$  days. (Bottom row) The spectral distributions of vorticity ( $\mathcal{Z}$ ) and divergence ( $\mathcal{D}$ ) on day 7 of genesis in the (d) lower, (e) middle and (f) upper troposphere of RAMS and the reduced model with CB closure. The plotted values of  $\mathcal{E}_h$  ( $\mathcal{Z}$  and  $\mathcal{D}$ ) are normalized to the common maximum of  $\mathcal{E}_h$  ( $\mathcal{Z}$ ) in the boundary layer at  $t = 4.33$  days.

is another statistic which differentiates pre-hurricane turbulence in RAMS and the reduced model. This statistic may be derived from the time series of the following vorticity autocorrelation function:

$$A_\zeta(t, t') \equiv \frac{(\zeta_p - \bar{\zeta}_p)_t (\zeta_p - \bar{\zeta}_p)_{t'}}{\delta\zeta_p(t) \delta\zeta_p(t')}, \quad t' \geq t. \quad (26)$$

Here,  $\zeta_p(t)$  is the relative vorticity measured by a passive tracer at time  $t$ . The variables  $\bar{\zeta}_p$  and  $\delta\zeta_p$  are the mean and standard deviation of  $\zeta_p$  over all tracers. Using the same convention, the overbar above the numerator denotes the mean over all tracers. The measurement of  $\zeta_p$  consists of a flat average of relative vorticity over all grid points in a horizontal square of length  $2nd$  centred on the tracer, in which  $d$  is the horizontal grid spacing and  $n$  is an integer. Here, we let  $n = 6$ , which tends to filter out the impact of grid scale fluctuations. The author has verified that results for  $n = 3$  are qualitatively similar.

At time  $t$ , one tracer is placed at each horizontal grid point of the boundary layer where the absolute value of  $\zeta$  exceeds some threshold. For the present analysis, we let this threshold equal twice the root-mean-square of  $\zeta_p$  (measured as described above) for a set of test particles that are temporarily placed on all grid points. Over time, the tracers move with the horizontal wind of the boundary layer. They are given no vertical velocity.

Figure 13(a) shows the decay of the autocorrelation  $A_\zeta$  in RAMS and in the reduced model with CB, BLQ and SB cumulus parametrizations, starting at  $t = 7$  days. The dashed curve corresponds to the reduced model,

stripped of both surface friction and cumulus convection. Figure 13(b) illustrates the density distributions of the pseudo-Lagrangian tracers at the start of the autocorrelation measurement, and at a later time. The tracer vorticity ‘decorrelates’ slowly in the stripped run, presumably due to an enstrophy cascade toward subgrid (dissipation) scales. Restoring surface friction and cumulus convection provides additional means to create and destroy vorticity, and therefore expedites the decorrelation. Notably,  $A_\zeta$  decays faster in the CB run than in the BLQ and SB runs. This result may reflect the faster acceleration of boundary layer winds in the CB simulation. A much faster decay of  $A_\zeta$  in the RAMS simulation seems consistent with the prevalence of short wave (sporadic and small-scale) storm structures in a CSR model. Exponential fits to  $A_\zeta$  give  $e$ -folding decay times of about 12 h for RAMS and 5–7 days for the reduced model. The fits are taken over the first 8 h and 24 h of the autocorrelation measurement for RAMS and the reduced model, respectively.

## 5. Conclusion

Reduced models have virtue in their simplicity, but oversimplification can produce misleading results instead of conceptual clarity. The purpose of this study was to evaluate the adequacy of a typical reduced (three-layer) model for understanding tropical cyclogenesis from turbulent initial conditions. To this end, the model was directly compared to tropical cyclogenesis in a standard CSR model (RAMS).

Table II summarizes the evaluation, based on past and present results. Earlier studies confirmed that the reduced model under consideration is capable of generating

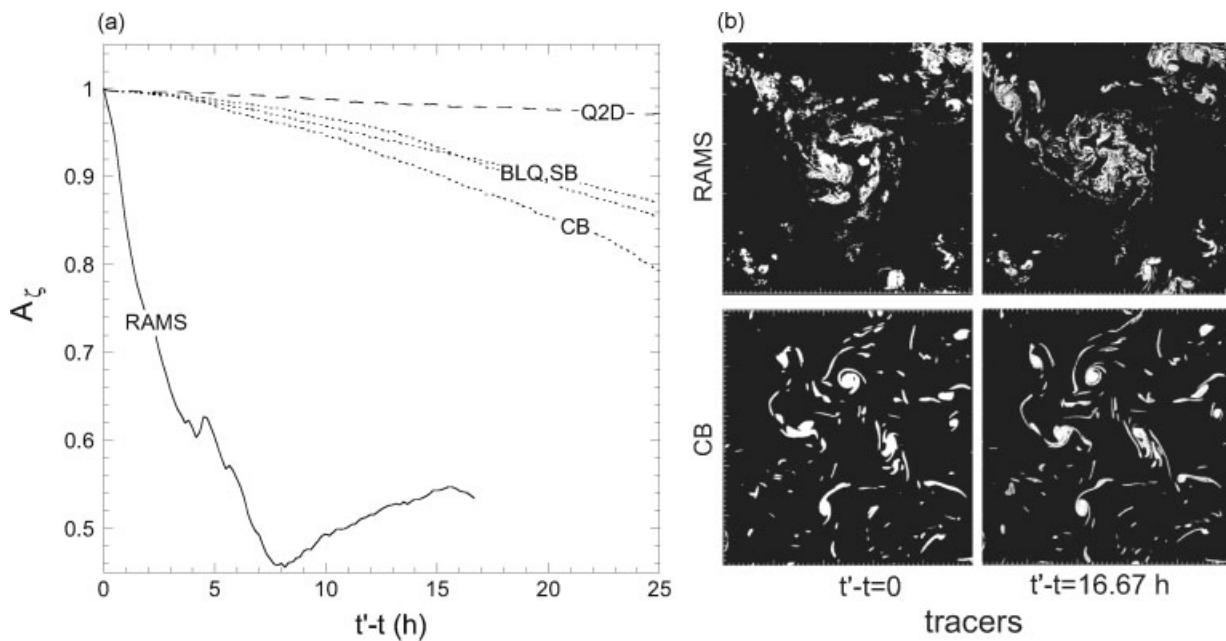


**Figure 13.** (a) The pseudo-Lagrangian autocorrelation of relative vorticity in the boundary layer starting at  $t = 7$  days. The solid curve corresponds to the RAMS simulation, and the dotted curves correspond to the reduced model with CB, BLQ and SB closures. The dashed curve corresponds to the reduced model with no surface fluxes, no cumulus parametrization, and no radiation, resulting in quasi-two-dimensional (Q2D) dynamics. The plots in (b) show the number density of pseudo-Lagrangian tracers in the ensemble used to compute the autocorrelation in RAMS (top row) and the reduced model with CB closure (bottom row). White corresponds to a density greater than or equal to one tracer per grid cell. The black space is devoid of tracers. The tracers are initially located in regions of high relative vorticity (see text). Each panel shows the entire horizontal domain.

realistic hurricanes, whose intensities increase with the SST and the ratio  $C_E/C_D$  (between zero and realistic values). Earlier studies also showed that the reduced model appropriately accelerates hurricane formation with increasing  $C_E$  or SST. The influence of surface friction on the rate of tropical cyclogenesis may depend on circumstances. Here, we considered a CSR simulation in which removing surface friction appears to completely suppress hurricane formation in turbulence over a relatively cool ocean. Suppression also occurs in the reduced model, when the cumulus parametrization constrains the upward mass flux to scale in direct proportion to the convergence of unstable air in the boundary layer. If instead the mass flux receives a selective boost in regions of exceptionally high instability, or is governed by boundary layer quasi-equilibrium, hurricanes develop without surface friction in the reduced model, after a relatively long time period.

For cases in which tropical storms become hurricanes, the process of rapid intensification appears similar in both the CSR and reduced models. The onset coincides with pronounced growth of  $\eta$  in convectively active regions. The growth of  $\eta$  is associated with local elevation of moist entropy in the lower and middle troposphere. The vortex evolves from a state of substantial convective instability to one of quasi-neutrality in the eyewall, after which there is no further amplification of the maximum wind speed.

Nevertheless, the details of pre-hurricane turbulence differ considerably between the reduced and CSR models. In the CSR model, pre-hurricane turbulence is relatively energetic for horizontal wavelengths less than 100 km. The boundary layer flow is substantially more divergent in the intermediate mesoscale, as are the flows along pressure isosurfaces in the middle and upper troposphere. Furthermore, the vorticity autocorrelation decays relatively

fast in areas of strong rotation. By contrast, the reduced model filters out intense, small-scale storm features. Such smoothing results in a simplified (quasi-2D) form of rotational convective turbulence. The cyclonic vortices within the simplified turbulence are robust compared to their counterparts in the CSR model. As a result, more become tropical cyclones, before merging into a single strong hurricane.

In conclusion, we have seen that hurricane formation in the reduced and CSR models occur through analogous air–sea interaction instabilities. However, spectral discrepancies with the CSR model suggest that the reduced model inaccurately simulates the input, output and/or transfer of energy in the small to intermediate mesoscale regime of pre-hurricane turbulence. While ‘short wave’ deficiencies may not profoundly influence the time-scale of hurricane formation, they certainly effect the precise time and location where rapid intensification is triggered. Conceivably, fine tuning of parameters might converge the spectral characteristics of the reduced and CSR models. However, a better cumulus parametrization, variable boundary layer depth, and some degree of stochastic forcing in the reduced model may be necessary.

#### Acknowledgements

This work was supported by NSF grant ATM-0750660. The author thanks Dr Melville Nicholls for a helpful discussion on how to modify the surface flux parametrization in RAMS. The author also thanks two anonymous reviewers for their constructive feedback on the original manuscript.

Table II. 'Report card' for the reduced (three-layer) model with basic cumulus parametrizations.

Subject	Comparison of cloud-system-resolving (CSR) and reduced models	Provisional grade of reduced model	Select references
Steady-state intensity	In the reduced model, the maximum wind speed decreases with the SST and $C_E/C_D$ , as expected from traditional hurricane theory; recent CSR simulations and theoretical considerations suggest less (and sometimes opposite) sensitivity to realistic variation of $C_D$ ; the reduced model tends to produce weaker storms.	Fair	O69; E86; RE87; SMV08; SM08; BR09a,b; SD09; S10; MSN10.
Basic steady-state structure	Both models produce hurricanes with warm-core structure, an overturning secondary circulation, and quasi-convective neutrality in the eyewall.	Good	O69; RE87; DP88; H93; Section 4.5; Figure 11.
Rapid intensification	In both models, the onset of intensification follows moist-thermodynamic preconditioning characterized by pronounced growth of $\eta$ ; intensification proceeds while the eyewall has substantial convective instability, and appears to stop when near-neutrality is achieved.	Good	O69, DP88, SD09; Sections 4.4, C; Figures 9, 10, C1.
$C_E$ and SST dependence of formation rate	In both models, increasing $C_E$ or the SST (all else being equal) accelerates hurricane formation; setting $C_E$ to zero generally quenches development.	Good	O69, SD09; Sections 2.1, 2.3, 4.3; Figures 1, 2.
$C_D$ dependence of formation rate	In both models, removing surface drag inhibits hurricane formation; hurricanes eventually form without surface drag in the reduced model with the BLQ or SB cumulus parametrization, but do not form in the CSR model or in the reduced model with CB closure.	Good	O69, SD09, FTW09, MSN10; Sections 2.2, 4.3; Figures 4, 8.
Number of tropical cyclones	One hurricane forms over a cool ocean in the CSR model; several tropical cyclones form in the reduced model, but later merge into one stronger hurricane.	Fair	Sections 2.1, 4.2; Figures 1(a), 2(top), 7.
Horizontal kinetic energy spectrum $\mathcal{E}_h$ of intermediate turbulence	For horizontal wavelengths between 30 and a few hundred km, the lower tropospheric $\mathcal{E}_h$ varies as $k^{-2}$ in the CSR model, but as $k^{-3}$ in the reduced model; accordingly, rotational convective turbulence in the CSR model maintains greater energy in the 'short wave' mesoscale; enhanced short wave energy is robust to vertical averaging of $\mathbf{u}$ .	Unsatisfactory	Sections 4.6, D; Figures 12, D1.
Divergence versus vorticity of the horizontal flow	For the aforementioned wavelengths, the spectral density of divergence $\mathcal{D}$ exceeds that of relative vorticity $\mathcal{Z}$ in the boundary layer of the CSR model, during the intermediate stage of tropical cyclogenesis; the ratio $\mathcal{D}/\mathcal{Z}$ is fragile to vertical averaging of $\mathbf{u}$ above the boundary layer; in all layers of the reduced model, $\mathcal{D}$ is less than $\mathcal{Z}$ .	Unsatisfactory	Sections 4.6, D; Figures 12, D1.
Vorticity autocorrelation	During genesis, the vorticity autocorrelation in regions of strong rotation decays more rapidly in the CSR model than in the reduced model; faster decay of the autocorrelation is consistent with unfiltered convection involving sporadic and severe storms.	Unsatisfactory	Section 4.7; Figure 13.

Full versions of the abbreviated references are mentioned in the text.

## Appendix A. Modified surface flux parametrization in RAMS

### 5.1. Formulation

The reader may consult Black *et al.* (2007) for a modern perspective on heat and momentum fluxes at the air–sea interface, and Walko *et al.* (2000) for a description of the standard surface flux parametrization of RAMS. For the present study, the surface momentum flux is simplified to:

$$\tau_{\mathbf{u}} = -C_{D*} (a + b |\mathbf{u}_+|) |\mathbf{u}_+| \mathbf{u}_+. \quad (\text{A1})$$

Likewise, the potential temperature and water vapour fluxes are simplified to:

$$\begin{aligned} \tau_{PT} &= C_{E*} (a + b |\mathbf{u}_+|) |\mathbf{u}_+| (\theta_s - \theta_+), \\ \tau_{r_v} &= C_{E*} (a + b |\mathbf{u}_+|) |\mathbf{u}_+| (r_{vs}^* - r_{v+}). \end{aligned} \quad (\text{A2})$$

Here, the variables  $\mathbf{u}_+$ ,  $\theta_+$  and  $r_{v+}$  are the horizontal velocity, potential temperature and vapour mixing ratio at the first grid point above sea level. The variables  $\theta_s$  and  $r_{vs}^*$  are the potential temperature and saturation vapour mixing ratio at sea level. The parameters  $C_{D*}$  and  $C_{E*}$  have adjustable values, whereas  $a = 0.0011$  and  $b = 4 \times 10^{-5} \text{ m s}^{-1}$ . Note that letting  $C_{D*} = 1$  yields Deacon's relation for the momentum flux (e.g. Moss and Rosenthal, 1975).

Let  $h_0$  denote the height of the top of the boundary layer, where (for simplicity) turbulent fluxes are assumed to be negligible compared to their values at the surface. Furthermore, suppose that  $\mathbf{u}_+$  differs only slightly from the vertically averaged horizontal velocity  $\mathbf{u}_0$  in the boundary layer. Then, the acceleration of  $\mathbf{u}_0$  due to the surface flux (sf) is given by

$$\left( \frac{d\mathbf{u}_0}{dt} \right)_{\text{sf}} \approx -\frac{C_{D*}}{h_0} (a + b |\mathbf{u}_0|) |\mathbf{u}_0| \mathbf{u}_0, \quad (\text{A3})$$

which is equivalent to the formula used in the reduced model. Further suppose that  $\theta_+$  and  $r_{v+}$  differ only slightly from the vertical averages of the potential temperature  $\theta_0$  and vapour mixing ratio  $r_{v0}$  in the boundary layer. Then,

$$\begin{aligned} \left( \frac{d\theta_0}{dt} \right)_{\text{sf}} &\approx \frac{C_{E*}}{h_0} (a + b |\mathbf{u}_0|) |\mathbf{u}_0| (\theta_s - \theta_0), \\ \left( \frac{dr_{v0}}{dt} \right)_{\text{sf}} &\approx \frac{C_{E*}}{h_0} (a + b |\mathbf{u}_0|) |\mathbf{u}_0| (r_{vs}^* - r_{v0}). \end{aligned} \quad (\text{A4})$$

Equations (A4) may be used to construct an auxiliary equation for the surface forcing of boundary layer EPT. The differential of  $\theta_e$  (in the absence of condensate) is expressible as

$$d\theta_e = \left( \frac{\partial \theta_e}{\partial \theta} \right)_{r_v, p} d\theta + \left( \frac{\partial \theta_e}{\partial r_v} \right)_{\theta, p} dr_v + \left( \frac{\partial \theta_e}{\partial p} \right)_{r_v, \theta} dp. \quad (\text{A5})$$

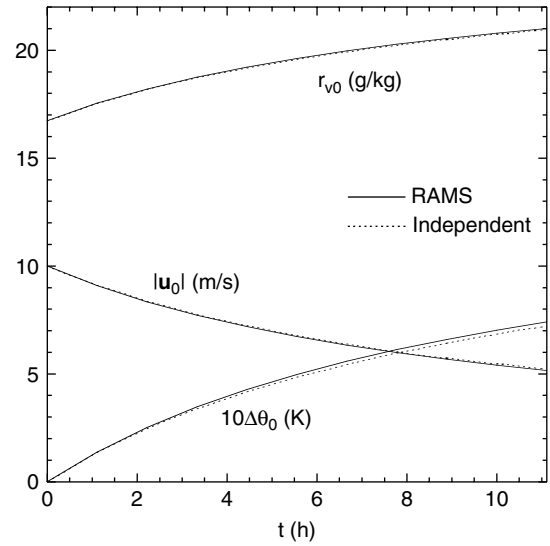


**Figure A1.** Time series of the horizontal wind speed ( $|\mathbf{u}_0|$ ), vapour mixing ratio ( $r_{v0}$ ) and change of potential temperature ( $\Delta\theta_0$ ) at the first level above the surface. The solid curves show RAMS output, and the dotted curves show an independent numerical solution of Eqs. (A3) and (A4).

Equations (A5) and (A4) imply:

$$\begin{aligned} \left( \frac{d\theta_{e0}}{dt} \right)_{\text{sf}} &= \left( \frac{\partial \theta_e}{\partial \theta} \right)_{r_v, p}^0 \left( \frac{d\theta_0}{dt} \right)_{\text{sf}} + \left( \frac{\partial \theta_e}{\partial r_v} \right)_{\theta, p}^0 \left( \frac{dr_{v0}}{dt} \right)_{\text{sf}} \\ &\approx \frac{C_{E*}}{h_0} (a + b |\mathbf{u}_0|) |\mathbf{u}_0| \\ &\quad \times \left[ \left( \frac{\partial \theta_e}{\partial \theta} \right)_{r_v, p}^0 (\theta_s - \theta_0) + \left( \frac{\partial \theta_e}{\partial r_v} \right)_{\theta, p}^0 (r_{vs}^* - r_{v0}) \right] \\ &\approx \frac{C_{E*}}{h_0} (a + b |\mathbf{u}_0|) |\mathbf{u}_0| (\theta_{es}^* - \theta_{e0}), \end{aligned} \quad (\text{A6})$$

in which the zero superscript means that the derivative is evaluated at  $\theta_0$ ,  $r_{v0}$  and  $p_0$ . The bottom line of Eq. (A6) is equivalent to the surface forcing of  $\theta_{e0}$  in the reduced model. It is derived by neglecting the small difference between the surface pressure  $p_s$  and the vertically averaged pressure  $p_0$  of the (thin) boundary layer.

### 5.2. Computational verification

Because hurricane formation is sensitive to the surface flux parametrization, it is necessary to demonstrate that the above modification is properly incorporated into the source code of RAMS. To test the code, we initialize RAMS with the Jordan (1958) mean sounding and uniform southwesterly winds of  $10 \text{ m s}^{-1}$ . The sea-surface temperature is set to  $29^\circ \text{C}$ , and the Coriolis parameter is set to zero. Radiation is turned off, and parametrized turbulence is reduced to a negligible level above the surface. The experiment is designed such that Eqs. (A3) and (A4) apply to field variables evaluated at the first grid point above sea level, with  $h_0$  given by the lowest vertical grid spacing. Solutions of Eqs. (A3) and (A4) are readily obtained by an independent procedure that combines analytical and numerical techniques. The procedure is straightforward, and the details are unimportant. Figure A1 compares the independent solution to RAMS output, and verifies that the surface flux modification is correctly implemented.

## Appendix B. Quasi-balanced initialization

### B1. Initialization of RAMS

The RAMS simulations are initialized with quasi-2D turbulence satisfying the following two balance conditions:

$$\nabla \cdot \mathbf{u} = 0 \quad \text{and} \quad \partial_t \nabla \cdot \mathbf{u} = 0, \quad (\text{B1})$$

in which  $\mathbf{u}$  is the horizontal velocity field. The vertical velocity is zero. Non-divergent horizontal flow permits one to write

$$\mathbf{u} = \hat{\mathbf{z}} \times \nabla \psi, \quad (\text{B2})$$

in which  $\psi$  is a standard stream function. Let  $(x, y, z)$  represent a Cartesian coordinate system in which  $z$  is the vertical coordinate. The stream function is related to the vertical vorticity  $\zeta \equiv \hat{\mathbf{z}} \cdot \nabla \times \mathbf{u}$  by the Poisson relation

$$\partial_{xx}\psi + \partial_{yy}\psi = \zeta. \quad (\text{B3})$$

In practice, we specify an initial vorticity field of the form

$$\zeta = \frac{\tilde{\zeta}(x, y)}{2} \left[ 1 + \tanh \left( \frac{10(h_c - z)}{h_c} \right) \right], \quad (\text{B4})$$

in which  $h_c = 6$  km. The Fourier modes of  $\tilde{\zeta}$ , whose horizontal wavelengths ( $2\pi/k$ ) fall between 500 and 25 km, are randomly generated in such a way that the enstrophy spectrum  $\mathcal{Z}(k)$  varies as  $k^{-1}$ . All other modes have zero amplitude. Equation (B3) with periodic boundary conditions is readily solved for  $\psi$ , and then Eq. (B2) is solved for  $\mathbf{u}$  at each vertical level.

The second balance constraint (combined with zero divergence) provides a Poisson equation for the perturbation Exner function  $\Pi'$ , in which  $\Pi \equiv c_{pd}(p/p_a)^{R_d/c_{pd}}$  and  $p_a = 10^3$  hPa. Taking the divergence of the horizontal velocity equation in RAMS, and enforcing both conditions in Eq. (B1) yields

$$\partial_{xx}\Pi' + \partial_{yy}\Pi' = \frac{2}{\theta_{va}} \left[ \partial_{xx}\psi \partial_{yy}\psi - (\partial_{xy}\psi)^2 \right] + \frac{f\zeta}{\theta_{va}}, \quad (\text{B5})$$

in which  $f$  is the Coriolis parameter and  $\theta_{va}$  is the ambient virtual potential temperature. Here, we have neglected frictional dissipation. Equation (B5) with periodic boundary conditions is readily solved for  $\Pi'$ . Hydrostatic balance is then used to calculate the virtual potential temperature perturbation:

$$\theta'_v = \frac{\theta_{va}^2}{g} \partial_z \Pi', \quad (\text{B6})$$

in which  $g$  is the gravitational acceleration.

### B2. Initialization of the reduced model

The initial horizontal velocity  $\mathbf{u}_m$  of layer  $m$  of the reduced model is obtained directly from the RAMS simulation in the early stage of genesis. The initial values of  $h_m$  (in the middle and upper layers) are obtained by neglecting  $\nabla \cdot \mathbf{u}_m$  and assuming the pressure gradient holds  $\partial_t \nabla \cdot \mathbf{u}_m$  equal to zero. Taking the divergence of the momentum equation (Eq. (2)),

ignoring cumulus forcing and friction, and imposing the balance conditions ( $\nabla \cdot \mathbf{u}_m = \partial_t \nabla \cdot \mathbf{u}_m = 0$ ) on layers 1 and 2 yields

$$\begin{aligned} \partial_{xx}h_1 + \partial_{yy}h_1 &= \frac{B_1 - \epsilon B_2}{g(1 - \epsilon)}, \\ \partial_{xx}h_2 + \partial_{yy}h_2 &= \frac{B_2 - B_1}{g(1 - \epsilon)}. \end{aligned} \quad (\text{B7})$$

Here, we have introduced the source variable

$$B_m \equiv f\zeta_m + 2(\partial_{xx}\psi_m)(\partial_{yy}\psi_m) - 2(\partial_{xy}\psi_m)^2, \quad (\text{B8})$$

in which  $\zeta_m \equiv \hat{\mathbf{z}} \cdot \nabla \times \mathbf{u}_m$  is the relative vorticity of layer  $m$  and  $\psi_m$  is the stream function of the non-divergent component of  $\mathbf{u}_m$ . As usual, the vorticity and stream function are related by  $\partial_{xx}\psi_m + \partial_{yy}\psi_m = \zeta_m$ . The top and bottom lines of Eq. (B7) are readily solved with periodic boundary conditions, and the requirement that  $\langle h_m \rangle = H_m$ .

## Appendix C. Structural evolution of the tropical cyclone in RAMS

This appendix briefly elaborates on tropical cyclone intensification in RAMS. Figure C1 shows the azimuthally averaged structure of the incipient hurricane of Figure 1(a) (as opposed to the broader circulation) as it rapidly intensifies into a mature storm. The centre of the vortex here corresponds to the point of minimum surface pressure. The contour plots are shown in the  $M$ - $z$  plane, in which  $M$  is absolute angular momentum and  $z$  is vertical distance from the sea surface. The absolute angular momentum is defined by

$$M \equiv r\bar{v} + \frac{fr^2}{2}, \quad (\text{C1})$$

in which  $r$  is the radius and  $\bar{v}(r, z, t)$  is the azimuthally averaged azimuthal velocity of the vortex. The value of  $M$  increases monotonically with  $r$  out to a  $z$ -dependent turning point. The field variables are not plotted beyond this point.

The top row of Figure C1 illustrates the evolution of the azimuthal and vertical velocities. Initially, the azimuthal velocity possesses a (short-lived) mid-level maximum. The inner core contains a narrow, central downdraught surrounded by a broader updraught. Both features are peaked in the upper troposphere, but only the updraught extends to the sea surface. In the mature storm, the azimuthal velocity is maximal near the surface; the vertical winds consist of a classic eyewall updraught surrounding an inner downdraught.

The bottom row of Figure C1 shows the evolution of the equivalent potential temperature (EPT) and the saturation EPT. The EPT is defined here by the formula (Emanuel, 1994)

$$\begin{aligned} \theta_e &\equiv T \left( \frac{p_r}{p - e} \right)^{R_d/(c_{pd} + c_{qr})} \left( \frac{e}{e^*} \right)^{-r_v R_v / (c_{pd} + c_{qr})} \\ &\times \exp \left\{ \frac{L_v r_v}{(c_{pd} + c_{qr}) T} \right\}, \end{aligned} \quad (\text{C2})$$

in which  $T$  is absolute temperature,  $p$  is total pressure,  $p_r = 1000$  hPa,  $e$  and  $e^*$  are the actual and saturation vapour

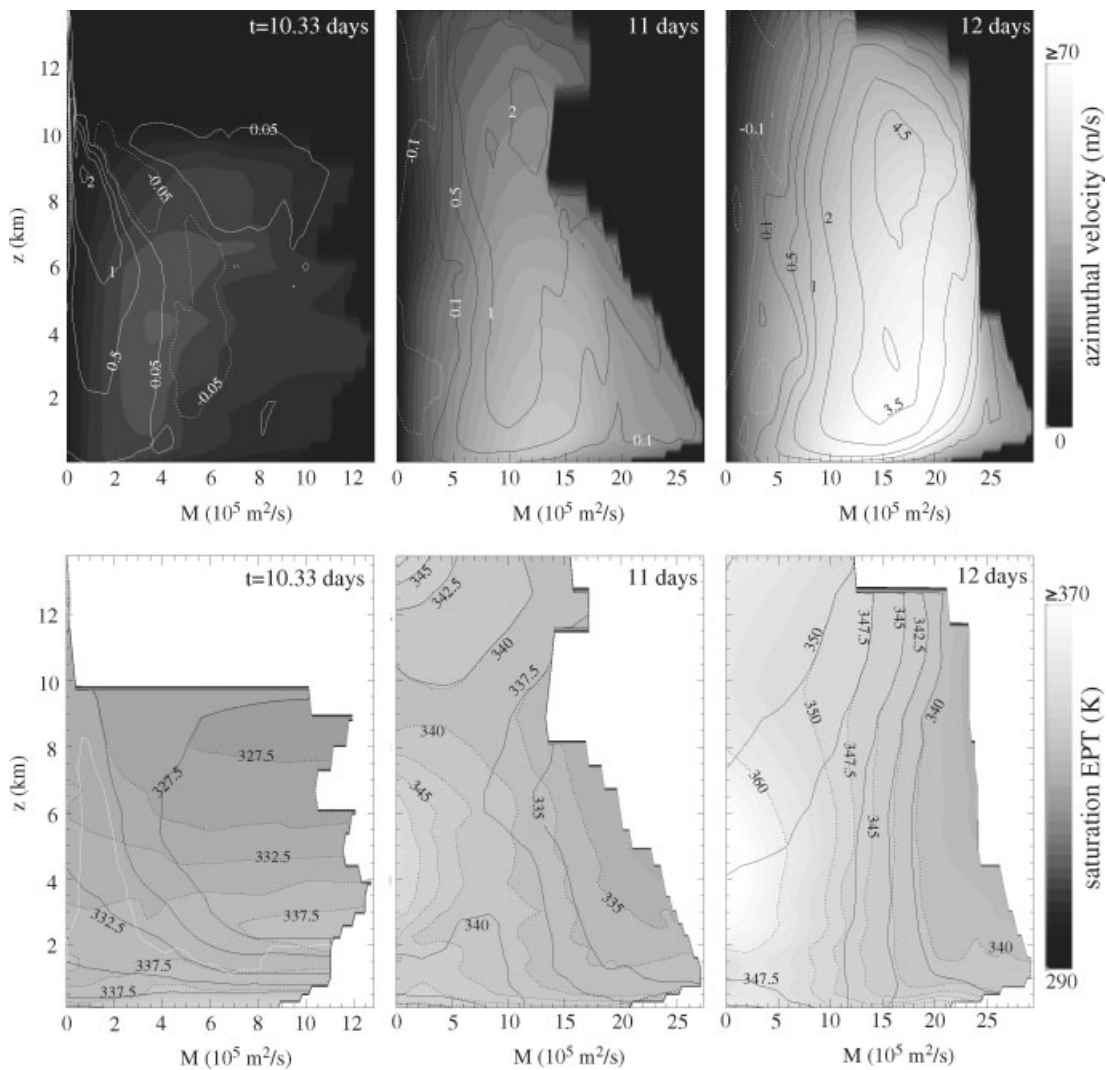


**Figure C1.** Evolution of vortex structure during rapid intensification in a RAMS simulation. (Top row) Azimuthally averaged tangential velocity (shading) and vertical velocity (contours), both in  $\text{m s}^{-1}$ , at 10.33, 11 and 12 days. (Bottom row) azimuthally averaged saturation EPT (shading, dotted contours) and EPT (solid black contours), both in K, at the same times. The maximum EPT along the azimuthal averaging circuit is no less than 335 K below the white contour in the lower left plot. Field variables are not mapped beyond the radius  $r(z)$  where  $\partial_r M = 0$ ; regions without data are black and white in the upper and lower plots, respectively.

pressures,  $r_v$  and  $r_t$  are the vapour and total mixing ratios,  $R_d$  and  $R_v$  are the gas constants of dry air and water vapour,  $c_{pd}$  is the isobaric specific heat of dry air,  $c_l$  is the specific heat of liquid water, and  $L_v$  is the latent heat of vaporization. As the vortex begins to intensify, the azimuthally averaged boundary layer EPT exceeds the saturation EPT in the middle to upper tropospheric region of the central updraught. Therefore, exploitable CAPE is evident in the mean profile. Equilibration coincides with the establishment of approximate slantwise convective neutrality (a substantial reduction of slantwise CAPE) in the main updraught. Perfect neutrality would correspond to overlapping isosurfaces of saturation EPT and angular momentum, with saturated conditions above the boundary (subcloud) layer.

#### Appendix D. The effects of vertical averaging on the spectral characteristics of pre-hurricane turbulence in RAMS

The horizontal kinetic energy, vorticity and divergence spectra of pre-hurricane turbulence in RAMS are sensitive

to vertical averaging of the velocity fields. Let  $\bar{\mathbf{u}}_1^z(x, y)$  and  $\bar{\mathbf{u}}_2^z(x, y)$  denote the mass-weighted vertical averages of the horizontal velocity field  $\mathbf{u}$  in the middle layer ( $1 \text{ km} \leq z \leq 6 \text{ km}$ ) and upper layer ( $6 \text{ km} \leq z \leq 11 \text{ km}$ ) of RAMS, respectively. Figure D1(a) compares  $\mathcal{E}_h$  of  $\bar{\mathbf{u}}_m^z$  to  $\mathcal{E}_h$  of the reduced model with CB closure. For reference, the figure also plots  $\mathcal{E}_h$  of  $\mathbf{u}$  on the 700 and 300 hPa pressure isosurfaces of RAMS. The data correspond to  $t = 7$  days in the tropical cyclogenesis simulations of section 4 (cf. Figure 12).

As expected, vertical averaging lowers  $\mathcal{E}_h$  of RAMS toward that of the reduced model. However, the energy density stays relatively high for  $\Lambda < 100 \text{ km}$ . Doubling the resolution of the reduced model lowers viscosity and elevates  $\mathcal{E}_h$  at small scales, but not enough to match the RAMS spectra of the vertically averaged velocity fields.

Figure D1(b) plots  $\mathcal{Z}$  and  $\mathcal{D}$  of  $\bar{\mathbf{u}}_m^z$ . In contrast to horizontal flow on a pressure isosurface, the vertically averaged flow of a given layer is vorticity ‘dominant’ in the intermediate mesoscale. This result suggests that the divergence field of pre-hurricane turbulence in RAMS has less coherent vertical structure than the vorticity field.

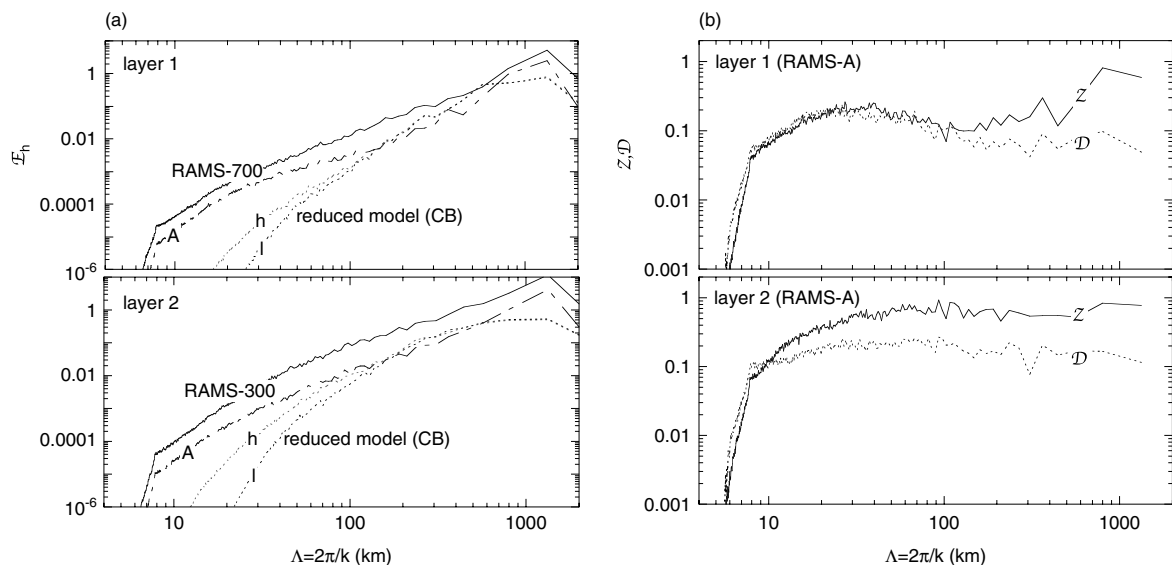


**Figure D1.** Sensitivity to vertical averaging. (a) Kinetic energy spectrum  $\mathcal{E}_h$  of the horizontal flow in layers 1 and 2, at  $t = 7$  days. The dashed-dotted curves (labelled A) correspond to vertically averaged flows, whereas the solid curves correspond to flows along the 700 and 300 hPa pressure isosurfaces of the RAMS simulation. The dotted curves correspond to the CB version of reduced model with ‘low’ (l) and ‘high’ (h) resolution, i.e. 3.9 km and 2 km horizontal grid spacing. (b) Spectral distributions of vorticity ( $\mathcal{Z}$ ) and divergence ( $\mathcal{D}$ ) of the vertically averaged flows in RAMS, at  $t = 7$  days. The normalizations in (a) and (b) are equivalent to those used in Figure 12.

## References

- Arakawa A. 2004. The cumulus parameterization problem: Past, present and future. *J. Climate* **17**: 2494–2525.
- Black PG, D’Asaro EA, French JR, Drennan WM, Niller PP, Sanford TB, Terrill EJ, Walsh ED, Zhang JA. 2007. Air–sea exchange in hurricanes: Synthesis of observations from the Coupled Boundary Layer Air–Sea Transfer Experiment. *Bull. Amer. Meteorol. Soc.* **88**: 357–374.
- Bouchut F, Lambaerts J, Lapeyre G, Zeitlin V. 2009. Fronts and nonlinear waves in a simplified shallow-water model of the atmosphere with moisture and convection. *Phys. Fluids* **21**: 116604.
- Braun SA, Tao W-K. 2000. Sensitivity of high-resolution simulations of hurricane *Bob* (1991) to planetary boundary-layer parameterizations. *Mon. Weather Rev.* **128**: 3941–3961.
- Bryan G, Rotunno R. 2009a. The maximum intensity of tropical cyclones in axisymmetric numerical model simulations. *Mon. Weather Rev.* **137**: 1770–1789.
- Bryan G, Rotunno R. 2009b. Evaluation of an analytical model for the maximum intensity of tropical cyclones. *J. Atmos. Sci.* **66**: 3042–3060.
- Carnevale GF, McWilliams JC, Pomeau Y, Weiss JB, Wang WR. 1991. Evolution of vortex statistics in two-dimensional turbulence. *Phys. Rev. Lett.* **66**: 2735–2738.
- Camargo SJ, Emanuel KA, Sobel AH. 2007a. Use of a genesis potential index to diagnose ENSO effects on tropical cyclone genesis. *J. Climate* **20**: 4819–4834.
- Camargo SJ, Sobel AH, Barnston AG, Emanuel KA. 2007b. Tropical cyclone genesis potential index in climate models. *Tellus A* **59**: 4428–4443.
- Charney JG, Eliassen A. 1964. On the growth of the hurricane depression. *J. Atmos. Sci.* **21**: 68–75.
- Cotton WR, Pielke Sr RA, Walko RL, Liston GE, Tremback CJ, Jiang H, McAnelly RL, Harrington JY, Nicholls ME, Carrio GC, McFadden JP. 2003. RAMS 2001: Current status and future directions. *Meteorol. Atmos. Phys.* **82**: 5–29.
- Craig GC, Gray SL. 1996. CISK or WISHE as the mechanism for tropical cyclone intensification. *J. Atmos. Sci.* **53**: 3528–3540.
- Crum FX, Dunkerton TJ. 1992. Analytic and numerical models of wave-CISK with conditional heating. *J. Atmos. Sci.* **49**: 1693–1708.
- Crum FX, Dunkerton TJ. 1993. CISK and evaporation-wind feedback with conditional heating on an equatorial beta-plane. *J. Meteorol. Soc. Japan* **72**: 11–18.
- Danilov SD, Gurarie D. 2000. Quasi-two-dimensional turbulence. *Physics-Uspekki* **43**: 863–900.
- DeMaria M, Pickle JD. 1988. A simplified system of equations for simulating tropical cyclones. *J. Atmos. Sci.* **45**: 1542–1554.
- DeMaria M, Schubert WH. 1984. Experiments with a spectral tropical cyclone model. *J. Atmos. Sci.* **41**: 901–924.
- DeMaria M, Knaff JA, Connell BH. 2001. A tropical cyclone genesis parameter for the tropical Atlantic. *Weather Forecast.* **16**: 219–233.
- DeMaria M, Mainelli M, Shay LK, Knaff JA, Kaplan J. 2005. Further improvement to the Statistical Hurricane Intensity Prediction Scheme (SHIPS). *Weather Forecast.* **20**: 531–543.
- Dengler K, Reeder MJ. 1997. The effects of convection and baroclinicity on the motion of tropical cyclone-like vortices. *Q. J. R. Meteorol. Soc.* **123**: 699–725.
- Dritschel DG, Waugh DW. 1992. Quantification of the inelastic interaction of unequal vortices in two dimensional vortex dynamics. *Phys. Fluids A* **4**: 1737–1744.
- Dunkerton TJ, Montgomery MT, Wang Z. 2009. Tropical cyclogenesis in a tropical wave critical layer: Easterly waves. *Atmos. Chem. Phys.* **9**: 5587–5646.
- Eliassen A. 1952. Slow thermally or frictionally controlled meridional circulation in a circular vortex. *Astrophys. Norv.* **5**: 19–60.
- Emanuel KA. 1986. An air–sea interaction theory for tropical cyclones. Part I: Steady-state maintenance. *J. Atmos. Sci.* **43**: 585–604.
- Emanuel KA. 1989. The finite amplitude nature of tropical cyclogenesis. *J. Atmos. Sci.* **46**: 3431–3456.
- Emanuel KA. 1991. The theory of hurricanes. *Annu. Rev. Fluid Mech.* **23**: 179–196.
- Emanuel KA. 1994. *Atmospheric Convection*. Oxford Univ. Press: New York.
- Emanuel KA. 1995a. The behavior of a simple hurricane model using a convective scheme based on subcloud-layer entropy equilibrium. *J. Atmos. Sci.* **52**: 3960–3968.
- Emanuel KA. 1995b. Sensitivity of tropical cyclones to surface exchange coefficients and a revised steady-state model incorporating eye dynamics. *J. Atmos. Sci.* **52**: 3969–3976.
- Fang J, Zhang F. 2010. Initial development and genesis of hurricane *Dolly* (2008). *J. Atmos. Sci.* **67**: 655–672.
- Fang J, Tang J, Wu R. 2009. The effect of surface friction on tropical cyclone development. *Adv. Atmos. Sci.* **26**: 1146–1156.
- Frierson DMW, Majda AJ, Paulis OM. 2004. Large-scale dynamics of precipitation fronts in the tropical atmosphere: A novel relaxation limit. *Comm. Math. Sci.* **2**: 591–626.
- Gray WM. 1968. Global view of the origins of tropical cyclones. *Mon. Weather Rev.* **96**: 669–700.
- Gray SL, Craig GC. 1998. A simple theoretical model for the intensification of tropical cyclones and polar lows. *Q. J. R. Meteorol. Soc.* **124**: 919–947.
- Hack JJ, Schubert WH. 1986. Nonlinear response of atmospheric vortices to heating by organized convection. *J. Atmos. Sci.* **43**: 1559–1573.
- Hendricks EA, Montgomery MT, Davis CA. 2004. The role of ‘vortical’ hot towers in the formation of tropical cyclone *Diana*. *J. Atmos. Sci.* **61**: 1209–1232.
- Houze RA. 1993. *Cloud Dynamics*. Academic Press: San Diego.
- Houze RA, Lee WC, Bell MM. 2009. Convective contribution to the genesis of hurricane *Ophelia* (2005). *Mon. Weather Rev.* **137**: 2778–2800.

- Jordan CL. 1958. Mean soundings for the West Indies area. *J. Meteorol.* **15**: 91–97.
- Kaplan J, DeMaria M. 2003. Large-scale characteristics of rapidly intensifying tropical cyclones in the North Atlantic Basin. *Weather Forecast.* **18**: 1093–1108.
- Kieu CQ, Zhang DL. 2009. An analytical model for the rapid intensification of tropical cyclones. *Q. J. R. Meteorol. Soc.* **135**: 1336–1349.
- Khouider B, Majda AJ. 2007. A simple multicloud parameterization for convectively coupled tropical waves. Part II: Nonlinear simulations. *J. Atmos. Sci.* **64**: 381–400.
- Lansky IM, O'Neil TM, Schecter DA. 1997. A theory of vortex merger. *Phys. Rev. Lett.* **79**: 1479–1482.
- Lapeyre G, Held IM. 2004. The role of moisture in the dynamics and energetics of turbulent baroclinic eddies. *J. Atmos. Sci.* **61**: 1693–1710.
- Liu Y, Zhang DL, Yau MK. 1997. A multiscale numerical study of hurricane Andrew (1992). Part I: Explicit simulation and verification. *Mon. Weather Rev.* **125**: 3072–3093.
- Liu Y, Zhang DL, Yau MK. 1999. A multiscale numerical study of hurricane Andrew (1992). Part II: Kinematics and inner-core structures. *Mon. Weather Rev.* **127**: 2597–2616.
- Mapes BE. 2000. Convective inhibition, subgrid-scale triggering energy, and stratiform instability in a toy tropical wave model. *J. Atmos. Sci.* **57**: 1515–1535.
- Marin JC, Raymond DJ, Raga GB. 2009. Intensification of tropical cyclones in the GFS model. *Atmos. Chem. Phys.* **9**: 1407–1417.
- Melander MV, McWilliams JC, Zabusky NJ. 1987. Axisymmetrization and vorticity-gradient intensification of an isolated two-dimensional vortex through filamentation. *J. Fluid Mech.* **178**: 137–159.
- Melander MV, Zabusky NJ, McWilliams JC. 1988. Symmetric vortex merger in two dimensions – Causes and conditions. *J. Fluid Mech.* **195**: 303–340.
- Möller JD, Montgomery MT. 2000. Tropical cyclone evolution via potential vorticity anomalies in a three-dimensional balance model. *J. Atmos. Sci.* **57**: 3366–3387.
- Montgomery MT, Bell MM, Abernethy SD, Black M. 2006. Hurricane Isabel (2003). New insights into the physics of intense storms. Part I: Mean vortex structure and maximum intensity estimates. *Bull. Amer. Meteorol. Soc.* **87**: 1335–1347.
- Montgomery MT, Nicholls ME, Cram TA, Saunders AB. 2006. A vortical hot tower route to tropical cyclogenesis. *J. Atmos. Sci.* **63**: 355–386.
- Montgomery MT, Smith RK, Nguyen SV. 2010. Sensitivity of tropical cyclone models to surface exchange coefficients. *Q. J. R. Meteorol. Soc.* in press.
- Moss MS, Rosenthal SL. 1975. On the estimation of planetary boundary layer variables in mature hurricanes. *Mon. Weather Rev.* **103**: 980–988.
- Nguyen SV, Smith RK, Montgomery MT. 2008. Tropical cyclone intensification and predictability in three dimensions. *Q. J. R. Meteorol. Soc.* **134**: 563–582.
- Nolan DS. 2007. What is the trigger for tropical cyclogenesis? *Austral. Meteorol. Mag.* **56**: 241–266.
- Nolan DS, Rappin ED, Emanuel KA. 2007. Tropical cyclogenesis sensitivity to environmental parameters in radiative-convective equilibrium. *Q. J. R. Meteorol. Soc.* **133**: 2085–2107.
- Nolan DS, Rappin ED. 2008. *Geophys. Res. Lett.* **35**: L14805, Doi:10.1029/2008GL034147
- Ooyama K. 1969. Numerical simulation of the life cycle of tropical cyclones. *J. Atmos. Sci.* **26**: 3–40.
- Ooyama K. 1982. Conceptual evolution of theory and modeling of the tropical cyclone. *J. Meteorol. Soc. Japan* **60**: 369–379.
- Raymond DJ. 1995. Regulation of moist convection over the west Pacific warm pool. *J. Atmos. Sci.* **52**: 3945–3959.
- Raymond DJ. 1997. Boundary layer quasi-equilibrium (BLQ). In *The Physics of Parameterization of Moist Convection*, Smith RK. (ed.) Kluwer Academic. 387–397.
- Raymond DJ, Sessions SL, Fuchs Z. 2007. A theory for the spin-up of tropical depressions. *Q. J. R. Meteorol. Soc.* **133**: 1743–1754.
- Reasor PD, Montgomery MT, Bosart LF. 2005. Mesoscale observations of the genesis of hurricane Dolly (1996). *J. Atmos. Sci.* **62**: 3151–3171.
- Rotunno R, Emanuel KA. 1987. An air–sea interaction theory for tropical cyclones: Part II. Evolutionary study using a non-hydrostatic axisymmetric numerical model. *J. Atmos. Sci.* **44**: 542–561.
- Sadourny R. 1975. The dynamics of finite-difference models of the shallow-water equations. *J. Atmos. Sci.* **32**: 680–689.
- Schecter DA. 2003. Maximum entropy theory and the rapid relaxation of three-dimensional quasi-geostrophic turbulence. *Phys. Rev. E* **68**: 066309: 1–8.
- Schecter DA. 2010. Hurricane intensity in the Ooyama (1969) paradigm. *Q. J. R. Meteorol. Soc.* **136**: 1920–1926.
- Schecter DA, Dubin DHE. 1999. Vortex motion driven by a background vorticity gradient. *Phys. Rev. Lett.* **83**: 2191–2194.
- Schecter DA, Dubin DHE. 2001. Theory and simulations of vortex motion driven by a background vorticity gradient. *Phys. Fluids* **13**: 1704–1723.
- Schecter DA, Dunkerton TD. 2009. Hurricane formation in diabatic Ekman turbulence. *Q. J. R. Meteorol. Soc.* **135**: 823–838.
- Schecter DA, Montgomery MT. 2003. On the symmetrization rate of an intense geophysical vortex. *Dyn. Atmos. Oceans* **37**: 55–88.
- Schecter DA, Dubin DHE, Cass AC, Driscoll CF, Lansky IM, O'Neil TM. 2000. Inviscid damping of asymmetries on a two-dimensional vortex. *Phys. Fluids* **12**: 2397–2412.
- Schubert WH, Hack JJ. 1982. Inertial stability and tropical cyclone development. *J. Atmos. Sci.* **39**: 1687–1697.
- Schubert WH, Montgomery MT, Taft RK, Guinn TA, Fulton SR, Kossin JP, Edwards JP. 1999. Polygonal eyewalls, asymmetric eye contraction, and potential vorticity mixing in hurricanes. *J. Atmos. Sci.* **56**: 1197–1223.
- Shapiro LJ. 1992. Hurricane vortex motion and evolution in a three-layer model. *J. Atmos. Sci.* **49**: 140–153.
- Shapiro LJ. 2000. Potential vorticity asymmetries and tropical cyclone evolution in a moist three-layer model. *J. Atmos. Sci.* **57**: 3645–3662.
- Shapiro LJ, Willoughby HE. 1982. The response of balanced hurricanes to local sources of heat and momentum. *J. Atmos. Sci.* **39**: 378–394.
- Skamarock WC, Klemp JB. 1992. The stability of time-split numerical methods for the hydrostatic and the nonhydrostatic elastic equations. *Mon. Weather Rev.* **120**: 2109–2127.
- Smith RK. 2000. The role of cumulus convection in hurricanes and its representation in hurricane models. *Rev. Geophys.* **38**: 465–489.
- Smith RK, Montgomery MT. 2008. Balanced boundary layers used in hurricane models. *Q. J. R. Meteorol. Soc.* **134**: 1385–1395.
- Smith RK, Montgomery MT, Zhua H. 2005. Buoyancy in tropical cyclones and other rapidly rotating atmospheric vortices. *Dyn. Atmos. Oceans* **40**: 189–208.
- Smith RK, Montgomery MT, Vogl S. 2008. A critique of Emanuel's hurricane model and potential intensity theory. *Q. J. R. Meteorol. Soc.* **134**: 551–561.
- Smith RK, Montgomery MT, Nguyen SV. 2009. Tropical cyclone spin-up revisited. *Q. J. R. Meteorol. Soc.* **135**: 1321–1335.
- Tory KJ, Frank WM. 2010. Tropical Cyclone Formation. *Global Perspectives on Tropical Cyclones From Science to Mitigation*, ed. Chan JCL, Kepert JD. World Scientific: Singapore, pp. 55–91.
- Walko RL, Band LE, Baron J, Kittel TGF, Lammers R, Lee TJ, Ojima D, Pielke Sr RA, Taylor C, Tague C, Trembeck CJ, Vidale PL. 2000. Coupled atmosphere-biophysics-hydrology models for environmental modeling. *J. Appl. Meteorol.* **39**: 931–944.
- Wirth V, Dunkerton TJ. 2009. The dynamics of eye formation and maintenance in axisymmetric diabatic vortices. *J. Atmos. Sci.* **66**: 3601–3620.
- Yano J-I, McWilliams JC, Moncrieff MW. 1995. Hierarchical tropical cloud systems in an analog shallow-water model. *J. Atmos. Sci.* **52**: 1723–1742.
- Zehnder JA. 2001. A comparison of convergence- and surface-flux-based convective parameterizations with applications to tropical cyclogenesis. *J. Atmos. Sci.* **58**: 283–301.
- Zhu H, Smith RK. 2002. The importance of three physical processes in a minimal three-dimensional tropical cyclone model. *J. Atmos. Sci.* **59**: 1825–1840.
- Zhu H, Smith RK, Ulrich W. 2001. A minimal three-dimensional tropical cyclone model. *J. Atmos. Sci.* **58**: 1924–1925.